The scale-invariant covariance spectrum of brain-wide activity

Zezhen Wang[1,*], Weihao Mai[6,*], Yuming Chai[2,3,*], Kexin Qi[2,3], Hongtai Ren[4], Chen Shen[2,3], Shiwu Zhang[4], Guodong Tan[2], Yu Hu[5,6,✉], and Quan Wen[1,2,3,✉]

[1]School of Data Science, University of Science and Technology of China

[2]Division of Life Sciences and Medicine, University of Science and Technology of China, Hefei, China

[3]Hefei National Laboratory for Physical Sciences at the Microscale, Center for Integrative Imaging, University of Science and Technology of China, Hefei, China

[4]Department of Precision Machinery and Precision Instrumentation, University of Science and Technology of China, Hefei, China

[5]Department of Mathematics, The Hong Kong University of Science and Technology, Hong Kong SAR, China

[6]Division of Life Science, The Hong Kong University of Science and Technology, Hong Kong SAR, China

Summary

The structure of high-dimensional neural activity plays a pivotal role in various sensory and behavioral processes. Here, we analyze whole-brain calcium activity in larval zebrafish, captured by fast light-field volumetric imaging during hunting and spontaneous behavior. We find that brain-wide activity is distributed across many principal component dimensions described by the covariance spectrum. Intriguingly, this spectrum shows an invariance to spatial subsampling: That is, the distribution of the eigenvalues of a smaller and *randomly sampled* cell assembly is statistically similar to that of the entire brain. We propose that this property can be understood using a Euclidean random matrix model (ERM), where pairwise correlation between neurons can be mapped onto a distance function between two points in a low-dimensional functional space. We numerically and analytically calculate the eigenspectrum in our model and identify three key factors that lead to the experimentally observed scale invariance: (i) the slow decay of the distance-correlation function, (ii) the higher dimension of the functional space, and (iii) the heterogeneity of neural activity. Our theory can quantitatively recapitulate the scale-invariant spectrum in zebrafish data, as well as two-photon and multi-area electrode recordings in mice. Furthermore, fitting the model to the experimental data uncovers a reorganization of neurons in the functional space when the zebrafish is engaged in hunting behavior. Our results therefore provide new insights and interpretations of brain-wide neural activity and offer clues about circuit mechanisms for coordinating global neural activity patterns.

[*]Equal contribution

Correspondence: *mahy@ust.hk, qwen@ustc.edu.cn*

1 Introduction

Geometrical and statistical analyses of neuronal population activity have shed light on the hidden structures of neural representations and brain dynamics. Dimensionality reduction methods, which seek to identify collective variables or latent variables underlying neural populations, promise to provide a simplified view of high-dimensional neural data (1, 2). Their applications to optical and multi-electrode recordings have begun to reveal important mechanisms by which neural cell assemblies process sensory information (3–5), make decisions (6–8), and generate motor behaviors (9–11). The fundamental reason for thinking of neural computation in terms of a small number of collective variables is the ubiquitous observation of neural correlation, whose structure is shaped by the synaptic connectivity between neurons and the statistics of external stimuli (12, 13). A large body of work has focused on the correlation between neurons (14), which can be measured for a large number of neurons recorded simultaneously in a reasonable amount of time (15). Theoretical analyses of the nature and structure of correlation have implicated its detrimental or beneficial roles in information coding (16–20), as well as its central contribution to synaptic plasticity (21), memory formation, and attention (22–24).

Here, we study the pairwise correlation structure in brain-wide activity in larval zebrafish described by the covariance matrix, which contains fundamental information about population activity. The eigenvectors of the covariance matrix correspond to the principal components of Principal Component Analysis (PCA), one of the widely used dimensionality reduction methods. The *effective dimension* of the subspace spanned by the principal components (PCs) depends on the moments of covariance eigenvalues and, as such, has gained much recent interest. On the one hand, many experimental studies that focus on specific brain regions have observed low-dimensional trajectories of population neural dynamics when animals were engaged in instructed tasks (25, 26). On the other hand, recent analyses of brain-wide activity (27) in freely behaving roundworm *(Caenorhabditis elegans* (28), fruit fly (*Drosophila melanogaster*) (29), and mouse (*Mus musculus*) (30, 31) have revealed that movement- and behavior-related neural activity is distributed across many principal components.

Consistent with a high-dimensional geometry of neural activity, several recent studies discovered that the eigenvalues of the neural covariance matrix display an approximate power-law distribution (32–36). In particular, Meshulam and colleagues (32) associated this statistical feature with an *invariance across scales*. Inspired by the renormalization group (RG) theory in statistical physics, they implemented a process that involved iteratively combining neuron pairs with maximal correlation. This method allowed them to build neural assemblies at different scales within the mouse hippocampus. This particular approach has since been applied to larger datasets across different mouse brain regions such as the visual cortex, the somatosensory cortex, and the motor cortex (36). Remarkably, when they assembled neurons into cell groups in this manner, the resulting neural covariance matrices displayed size (or scale)-invariant eigenspectra. This discovery raises two intriguing questions. First, do the scale-invariant eigenspectra depend on a *special* procedure for organizing neurons? Second, under what *conditions* does the scale-invariant phenomenon arise?

Here, we analyze brain-wide Ca^{2+} activity in larval zebrafish during hunting or spontaneous behavior (Fig. 1A) captured by fast light-field microscopy (37). Interestingly, we find that in 6 animals, the neural covariance matrices of *randomly subsampled* cell assemblies appear statistically similar to that of the entire brain (Fig. 1F). The similarity is manifested by plotting the eigenvalues of the subsampled covariance matrices in descending order against their normalized ranks. The eigenvalue curves corresponding to different sizes nearly collapse onto each other except for the largest eigenvalue (Fig. 1G). We verify this observation in datasets recorded by different experimental methods, including light-sheet imaging of larval zebrafish (38), two-photon imaging of mouse visual cortex (31), and multi-area Neuropixels recording in the mouse (31).

The collapse of eigenspectra across randomly subsampled neural covariance matrices is a *non-trivial* phenomenon. For example, the eigenspectrum of Wishart matrix (i.e., $C = GG^T$, where G is a $N \times T$ random matrix with i.i.d. entries), i.e. Marchenko–Pastur law, does *not* display scale-invariance over random subsampling (Fig. 3A). We will delve into this point by considering different cases in subsequent sections. To explain the observed phenomenon, we model the covariance matrix of brain-wide activity by generalizing the Euclidean Random Matrix (ERM) (39) such that neurons correspond to randomly distributed points in a d-dimensional Euclidean space, and the pairwise correlation between neurons decays according to their distance in this functional space. A similar idea was noted briefly in (32), while a key difference is that we consider random subsampling rather than grouping neurons based on their correlation (32). Biologically, the model indicates that neurons that are physically remote may still be in the functional neighborhood due to long-range connections between them. Our analytical and numerical calculations point to three key factors that play crucial roles in contributing to the scale invariance of the eigenspectrum: the

slow decay of the distance-correlation function; the higher dimension of the functional space; the heterogeneity of neural activity levels across neurons. Building upon our theoretical results, we use multidimensional scaling (MDS) and a parameterized distance function to infer the coordinates of each neuron in the functional space, and we apply Canonical Correlation Analysis (CCA) to identify a relationship between the anatomical positions of neurons and their locations in the functional space. Intriguingly, we discover that the hunting behavior of larval zebrafish *reorganizes* neurons in this space. Taken together, our results provide a new perspective to interpret the scale-invariant brain-wide activity and unambiguously show its organizing principles, with unexplored consequences for neural computation.

2 Results

2.1 Statistical features of zebrafish brain-wide activity

We recorded *simultaneous* brain-wide Ca^{2+} activity at a volume rate of 10 Hz in head-fixed larval zebrafish using a fast eXtended light field microscope (XLFM) (37). The various behaviors of the fish, including their hunting attempts, were captured by a high-speed infrared camera (50 Hz) (Fig. 1A, B). Hunting behavior, which is composed of stereotyped motor sequences such as eye convergence and J turn, was triggered by the presence of a *live* paramecium whose direction of movement was precisely controlled by a magnetic field (S1). We recorded spontaneous brain activity and behaviors in the absence of sensory stimuli in one fish as a control. Approximately 2000 ROIs (1977.3 $\pm$ 677.1, mean $\pm$ SD) with mean $\pm$ SD of diameter 16.84 $\pm$ 8.51 μm were analyzed in each fish according to the spatiotemporal activity of each voxel (S1). These ROIs likely correspond to multiple nearby neurons with highly correlated activity. For the sake of exposition, from now on we refer to the ROIs as "neurons".

Across the six zebrafish in our dataset, the distribution of the neural activity covariance C_{ij} (Methods) is broad and positively biased with a long tail (Fig. 1C, and Fig. S1A-D for all animals and data sets from other studies). Brain-wide activity is also highly dimensional, requiring more than 250 dimensions to explain 50% of activity variance (Fig. 1D). Consistent with this notion, when the eigenvalues of the covariance matrix are arranged in descending order and plotted against the normalized rank r/N, where $r = 1, \ldots, N$, or the *rank plot*, the curve is approximately a power law $\lambda \sim (r/N)^{-\alpha}$, for the top 1% to 10% large eigenvalues (Fig. 1G, $\alpha = 0.47 \pm 0.08$, mean$\pm$SD, $R^2 = 97.2 \pm 1.5\%$, mean$\pm$SD, $n = 6$ fish). Most intriguingly, the eigenspectrum curves of smaller randomly subsampled covariance matrices (that is, the covariance matrix for N randomly chosen neurons) almost collapse with each other for a wide range of eigenvalues (except for around the first 1 to 5 eigenvalues, Fig. 1G). In particular, we can also directly visualize the similarity of the covariance matrices of randomly sampled neural populations (Fig. 1F) after properly rearranging the neuron indices (Methods).

This observation of *scale invariance* in the covariance matrix cannot be reproduced when we replace its eigenvectors (i.e., the principal components) with a random orthonormal basis while the eigenvalues are kept identical (Fig. 1H, see Methods). In particular, after the replacement of the eigenvector, the heterogeneity of diagonal entries (that is, the variance of neural activity) of the covariance matrix becomes much reduced (Fig. 1G,H, gray dots). We will revisit the implications of this observation in section 2.4.

2.2 ERM model

Dimension reduction methods such as MDS and tSNE (40, 41), have been widely used to analyze large-scale neural activity data by embedding neurons into a low-dimensional space to reveal functional organizations (38), with nearby neurons showing higher correlations than those further away. The Euclidean Random Matrix (ERM (39)) prescribes a generative model for the covariance matrix in reverse to these ideas of dimensionality reduction. Neurons are assumed to be uniformly randomly distributed in a d-dimensional functional space, $[0, L]^d$. The pairwise correlation between neurons i, j is determined by a *kernel function* $f(\vec{x}_i - \vec{x}_j)$, which is a decreasing function of their distance $\|\vec{x}_i - \vec{x}_j\|$ in this functional space and $f(0) = 1$. The model is also justified by observing a broad and largely positive distribution of covariances in our data (Fig. 1C). To model the covariance matrix, we extend the ERM by introducing heterogeneous variances σ_i^2 of neural activity. σ_i^2 are drawn i.i.d. from a given distribution and are independent of the neuron coordinates $\vec{x}_i$. In short, the covariance between neuron i and j is given by

$$C_{ij} = \sigma_i \sigma_j f(\vec{x}_i - \vec{x}_j), \quad i, j = 1, 2, \ldots, N. \tag{1}$$

We first explore the ERM with a few forms of $f(\vec{x})$ and find that fast decaying functions such as the Gaussian pdf $f(\vec{x}) = e^{-\|\vec{x}\|^2/(2\sigma_x^2)}$ and the exponential function $f(\vec{x}) = e^{-\|\vec{x}\|/(2b)}$ do not lead to eigenspectra similar to those observed in the data and no scale invariance over random subsampling (Fig. 3B,C,Fig. S3 and S3). Therefore, we

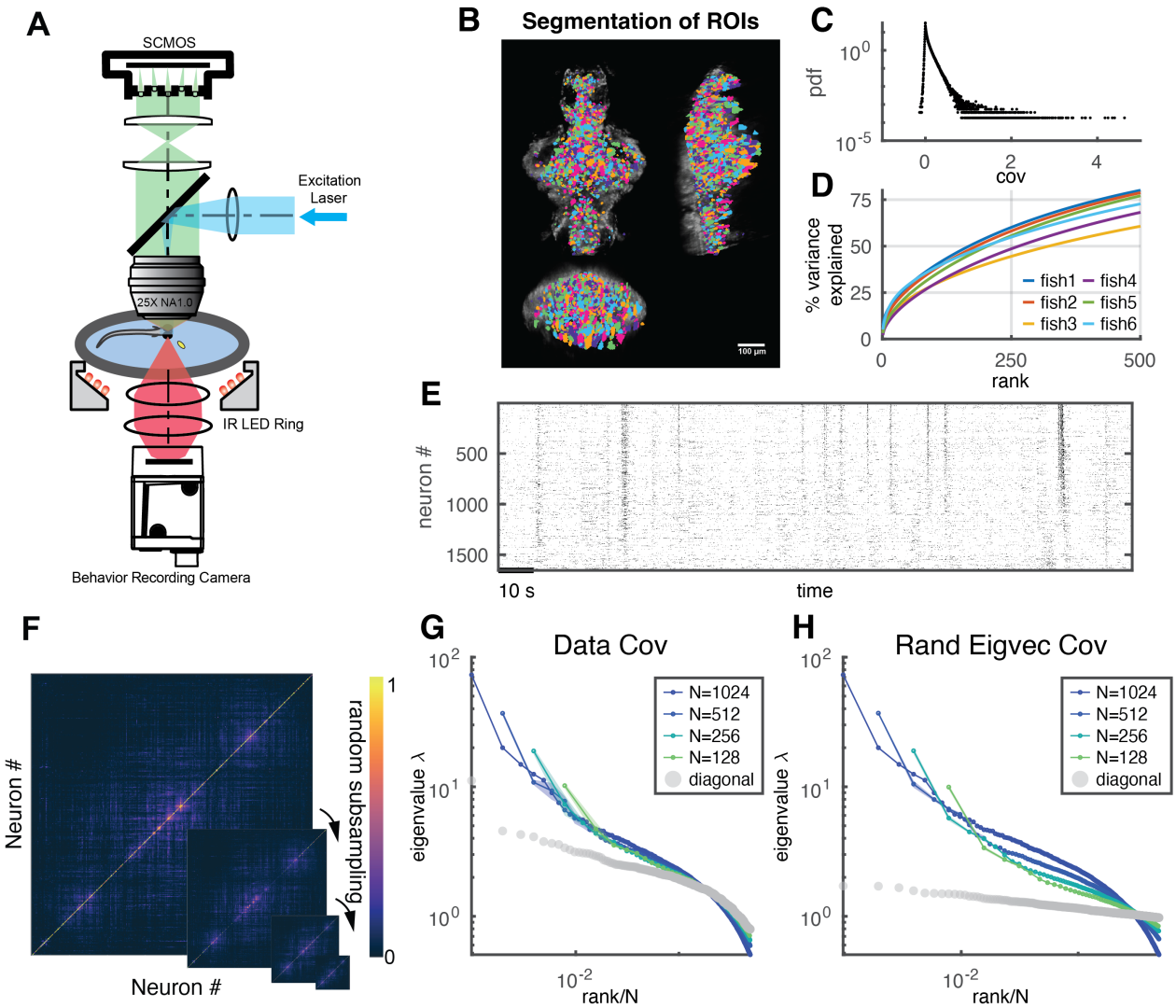

Figure 1. Whole brain imaging of zebrafish neural activity and the phenomenon of its scale-invariant eigenspectrum. **A.** Fast simultaneous light-field Ca^{2+} imaging of whole brain neural activity. **B.** Spatial distribution of segmented ROIs (shown in different colors). There are 1347 to 3086 ROIs in each animal. **C.** Distribution of normalized pairwise covariances in a representative fish. The mean of the diagonal entries of the covariance matrix is normalized to be 1. **D.** Explained variance of the activity data by PCs up to a given rank. The different colored lines represent different fish data (n=6). **E.** Example of a segment of brain-wide neural activity. The black dots represent the inferred firing rate. The ROIs are arranged according to their weightings on the first PC. The entire recording for each fish is 15.3±4.3 min (mean±SD). **F.** Iteratively subsampled covariance matrices. The ROI order in each subsampled covariance matrix is resorted such that entries near the diagonal exhibit higher covariance. **G. and H.** Subsampled covariance eigenspectra of an example fish data (**G**) and the covariance matrix constructed by substituting with random orthonormal eigenvectors (**H**). N is the number of neurons in the subsampled covariance matrix. The shaded area of each line represents the standard error of the mean (SEM). The rank plot is cut off after 503 of the largest eigenvalues; this is the number of principal components (PCs) required to explain 90% of the total variance.

focus on $f(\vec{x})$ with a slow decaying function such as the power-law tail $f(\vec{x}) \propto \|\vec{x}\|^{-\mu}$, which we find can produce qualitatively similar spectra to data (Fig. 2D,E). Since, by definition, $f(0) = 1$, the power law cannot hold near $x = 0$, and modifications are needed to avoid the singularity. Inspired by the Student's t-distribution, we adapt

$$f(\vec{x}) = \epsilon^{\mu}(\epsilon^2 + \|\vec{x}\|^2)^{-\mu/2}, \tag{2}$$

which approximates a power law $f(\vec{x}) \approx \epsilon^{\mu}\|\vec{x}\|^{-\mu}$ when $\|\vec{x}\| \gg \epsilon$ (Fig. 2B, C). There is a redundancy between the unit of the functional space (using a rescaled $\epsilon_\delta \equiv \epsilon/\delta$) and the unit of $f(\vec{x})$ (using a rescaled $f_\delta(\vec{x}) \equiv f(\vec{x}/\delta)$), so we arbitrarily set ϵ at a fixed value throughout this article.

Note that Eq. (2) is *not* the only form of slow decaying function that could lead to a scale-invariant covariance spectrum, as we will show below (Fig. S5). We choose the power-law function due to its analytical tractability in subsequent calculations of the eigenspectrum.

2.3 Two factors contribute to scale invariance

To understand under what conditions the scale invariance could arise from the covariance matrix generated as an ERM, we calculate the distribution of eigenvalues, or eigenspectrum, of C (Eq. (1)) analytically in the limit of $N \to \infty$, $L \to \infty$ by generalizing the replica method in (39). A key parameter is the neuron density $\rho := N/L^d$. In the *high-density* regime of $\rho \gg 1$, the probability density function (pdf) of the covariance eigenvalues can be approximated and expressed using the Fourier transform of the kernel function $\tilde{f}(\vec{k})$:

$$p(\lambda) = \frac{1}{\rho \mathrm{E}(\sigma^2)} \int_{\mathbb{R}^d} \frac{d^d\vec{k}}{(2\pi)^d} \delta\left(\frac{\lambda}{\mathrm{E}(\sigma^2)} - \rho\tilde{f}(\vec{k})\right), \tag{3}$$

where $\delta(x)$ is the Dirac delta function and $\mathrm{E}(\sigma^2)$ is the expected value of the variances of neural activity. Without loss of generality, here and below we set $\mathrm{E}(\sigma^2) = 1$ (for simulated and data matrix C, this means multiplying C by a constant such that $\mathrm{Tr}(C)/N = 1$). Intuitively, Eq. (3) means that λ/ρ are distributed with a density proportional to the area of $\tilde{f}(\vec{k})$' level sets (i.e., isosurfaces).

For the power-law kernel function $f(\vec{x})$ in Eq. (2), it is straightforward to use Eq. (3) to show that for large eigenvalues $\lambda \gg 1$, the eigenspectrum follows a power law (see a derivation in S3):

$$\begin{aligned} p(\lambda) &\sim \rho^{\frac{\mu}{d-\mu}} \lambda^{-\frac{2d-\mu}{d-\mu}}, \\ \text{and equivalently } \lambda &\sim (r/N)^{-1+\frac{\mu}{d}} \rho^{\frac{\mu}{d}}, \end{aligned} \tag{4}$$

where r is the rank of the eigenvalues in descending order. These equations provide intuitive explanations of the scale invariance over spatial subsampling. Note that subsampling in the ERM (Eq. (1)) is equivalent to reducing the density ρ. According to Eq. (4), the eigenspectrum becomes ρ-independent or scale-invariant when $\mu/d \to 0$. This predicts two factors that contribute to the scale invariance of the eigenspectrum. The first is a small exponent μ in the kernel function $f(\vec{x})$, which means that pairwise correlations slowly decay with functional distance and can be significantly positive across various functional modules and throughout the brain. Second, for a given μ, an increase in dimension d would improve the scale invariance. The dimension of the functional space d may be viewed as the neuronal coding space (33); it can also be related to the number of globally projecting latent variables (34) as an alternative interpretation (see also Discussion, S3).

We numerically verify our theoretical predictions of the two contributing factors to the scale invariance by directly comparing the subsampled eigenspectra in finite-size simulated ERMs across different combinations of μ and d (Fig. S4). Based on the discussion ensuing Eq. (3), here we consider the simplified case of $\sigma_i^2 = 1$ (we will revisit this later) in these simulations (Fig. 2D, E and Fig. S4). This also means that the entries of C are correlation coefficients. To quantitatively assess the scale invariance, we introduce a collapse index (CI) motivated by Eq. (4). In the log-log scale rank plot, Eq. (4) shows that the spectrum shifts vertically by $\frac{\mu}{d}\log\rho$ for large eigenvalues. Therefore, we define CI as this average displacement (smaller CI means more invariant):

$$\mathrm{CI} := \frac{1}{\log(q_0/q_1)} \int_{\log q_1}^{\log q_0} \left| \frac{\partial \log \lambda(q)}{\partial \log \rho} \right| \mathrm{d}\log q \tag{5}$$

Here $q_0, q_1 \in [0, 1]$ are fractions of eigenvalues (x-coordinate in Fig. 2D) chosen to select the range of large λ

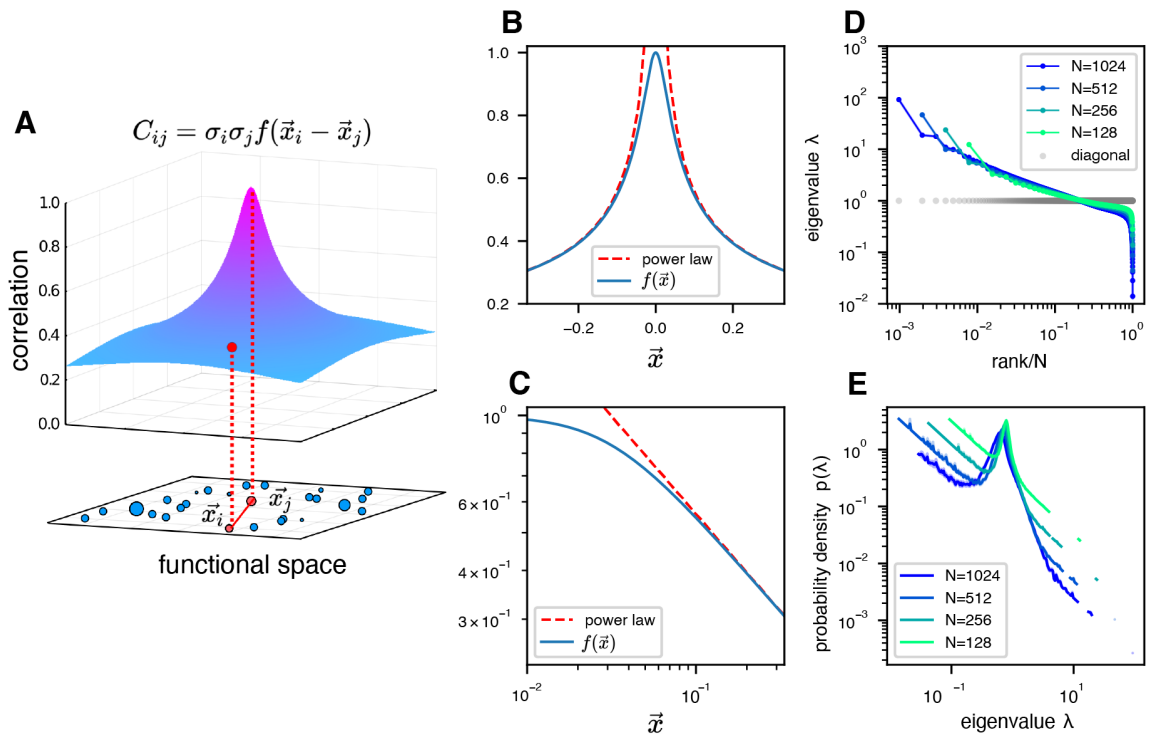

Figure 2. ERM model of covariance and its eigenspectrum. A. Schematic diagram of the ERM model. Bottom, the scattered blue circles represent the coordinates of neurons in a functional space $d = 2$. The bigger the circle, the greater its variance of neural activity σ_i^2. The solid line indicates the functional distance between two example neurons (red circles) and determines how strongly the two neurons are correlated according to the kernel function $f(\vec{x})$ (the surface above). The pairwise distance between two circles, as well as their corresponding sizes together, determine the covariance between the two neurons. **B.** Visualizing the slow-decaying kernel function $f(\vec{x})$ (solid blue line, Eq. (2)) and its power law asymptote (dashed red line) along a 1D slice. **C.** Same as **B** except on a log-log scale. **D.** Rank plots of eigenvalues for the ERM correlation matrix (that is, $\sigma_i^2 = 1$ in Eq. (1) as shown by the rank plot of diagonal entries in gray dots) over random subsampling (in green and blue). The original neuron size is $N = 1024$, $d = 2$, $L = 10$, $\rho = 10.24$ and $f(\vec{x})$ is given by Eq. (2) with $\mu = 0.5$ and $\epsilon = 0.03125$. The curves show the average of over 100 ERM simulations, and each ERM uses an identical subsample technique described in (Methods). The shaded area (most of which is smaller than the marker size) represents the SEM. **E.** Same as **D** but for probability density functions (pdfs).

as explained in the S1. For simulated ERMs and experimental covariance matrices, CI can be estimated using interpolation and quadrature.

Using Eq. (5), Fig. S4 confirms that the scale invariance improves with a slower correlation decay when μ decreases and when the functional dimension d increases. With a large μ and small d, the covariance eigenspectrum can vary with scale significantly (Fig. 3D and Fig. S4C,D,H).

Importantly, we find numerically that the two contributing factors to scale invariance – namely, slow spatial decay and high functional space – can be generalized to other *nonpower-law* functions. An example is the stretched exponential function $f(\vec{x}) = e^{-\|\vec{x}\|^{\eta}}$ with $0 < \eta < 1$. When η is small and d is large, the covariance eigenspectra also display a similar collapse upon random subsampling (Fig. S5).

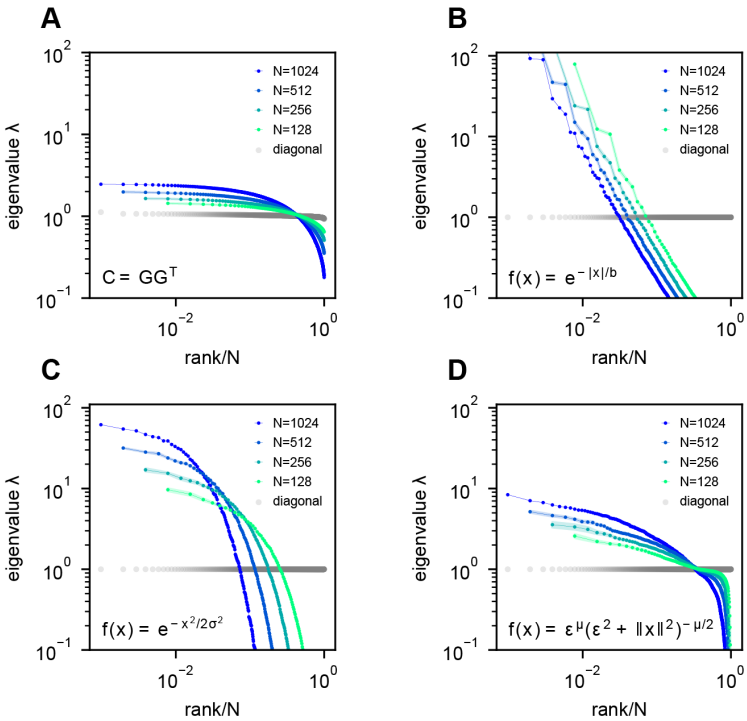

Figure 3. Eigenspectra collapse of the subsampled covariance matrices is a non-trivial result. **A.** Subsampled eigenvalue rank plot of the covariance matrix in the Marchenko-Pastur model, $N = 1024, T = 3072, \sigma = 1$. **B-D.** Subsampled eigenvalue rank plot of ERM with different functions $f(\vec{x})$. **B.** Exponential function $f(\vec{x}) = e^{-\|\vec{x}\|/b}$ where $b = 10$ and dimension $d = 2$. **C.** Gaussian pdf $f(\vec{x}) = e^{-\|\vec{x}\|^2/(2\sigma_x^2)}$ where $\sigma_x^2 = 1$ and dimension $d = 2$. **D.** Approximate power law Eq. (2) with $\mu = 0.9$ and dimension $d = 1$. **B-D** $\rho = 10.24$. Other parameters are the same as Fig. 2.

2.4 Heterogeneous activity levels across neurons enhance the scale invariance

So far, we have focused on the case of the covariance matrix with $\sigma_i^2 = 1$ in the ERM model (Eq. (1)), which means that C is a correlation matrix. It is then natural to check for any difference between the correlation and covariance matrix spectra. Using the introduced collapsed index (CI), we compare the level of scale invariance of the two spectra in the experimental data. Interestingly, we find that the CI of the covariance matrix is always smaller (i.e., more scale-invariant) across all the datasets (Fig. 4A, Fig. S6D, open *versus* closed squares), suggesting that the heterogeneity of neuronal activity variances σ_i^2 plays an important role in shaping the eigenspectrum.

This finding, however, cannot be explained by the high-density theory Eq. (3), which predicts that the eigenspectrum of the covariance matrix is simply a rescaling of the correlation eigenspectrum by $\mathrm{E}(\sigma_i^2)$, and the heterogeneity of σ_i^2 has no effect when $\rho \gg 1$. This theoretical prediction is indeed correct and is confirmed by direct numerical simulations and quantifying the scale invariance using the CI (Fig. S6A).

Fortunately, we can reconcile the discrepancy between the theory and the experimental data if we consider the ERM instead in the *intermediate-density* regime $\rho = O(1)$. Here, the resulting CI decreases with $\mathrm{E}(\sigma^4)$ (Fig. 4B), consistent with the observation in the experimental data. A better understanding of this phenomenon in

the regime $\rho = O(1)$ requires a more involved calculation of the eigenspectrum based on the Gaussian variational method (39), which specifies the eigenvalue pdf by a set of implicit equations that can be solved numerically (see Methods and S3). The variational method significantly improves the matching between the ERM simulations at intermediate ρ, where the high-density theory starts to deviate significantly (Fig. 4E,F, Fig. S2); the transition between these two regimes can also be understood (see Method and S3). Note that the departure of the leading eigenvalues in these plots is expected since the power-law kernel function we use is not integrable (see Methods for further elaborations). Furthermore, the scale invariance of the spectrum at $\mu/d \to 0$ previously derived using the high-density result (Eq. (4)) can be extended to the intermediate-density regime by proving the ρ-independence for the variational method (S3). Finally, using the variational method and the integration limit estimated by simulation (see S1), we show that the heterogeneity of population neural activity, quantified by $\mathrm{E}(\sigma^4)$ (recall that we fix $\mathrm{E}(\sigma^2) = 1$, Eq. (3)), indeed improves the collapse of the eigenspectra for intermediate ρ (S3). Our theoretical results agree excellently with the ERM simulation (Fig. 4B, S1).

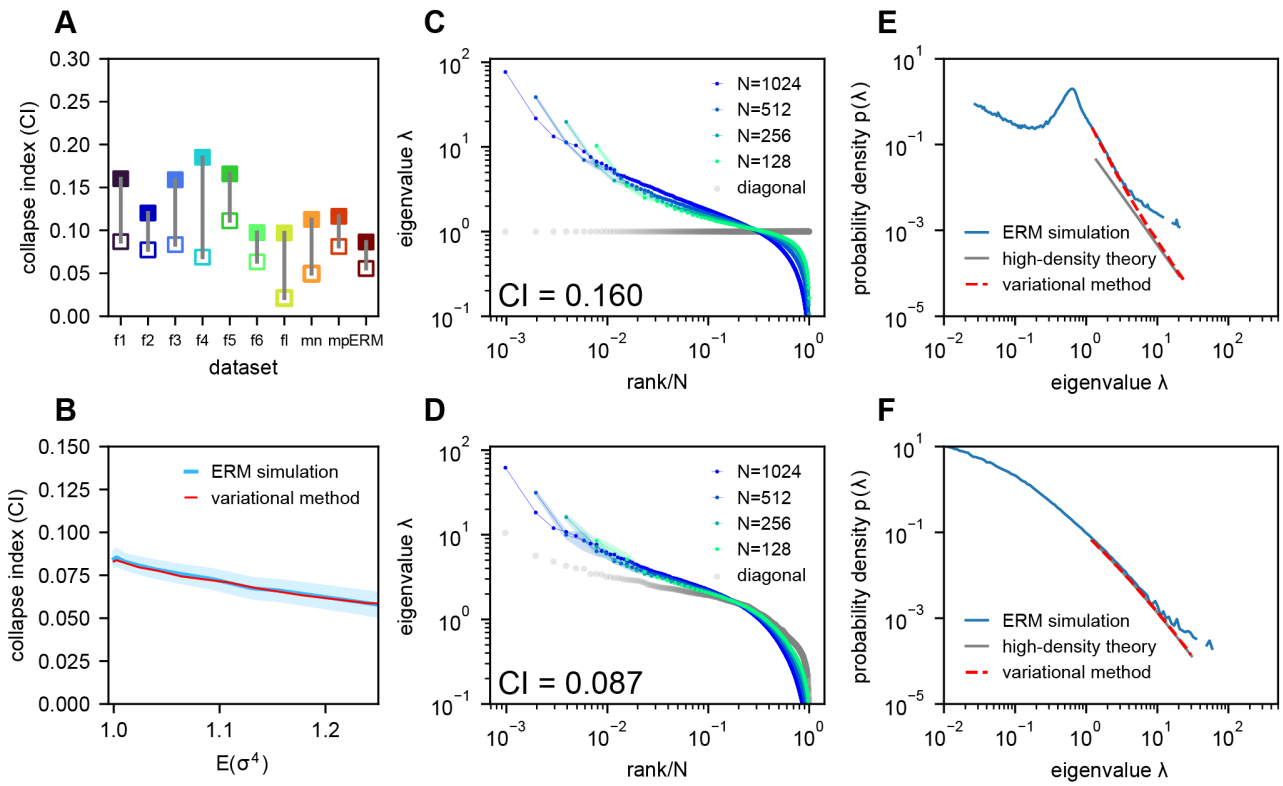

Figure 4. Impact of heterogeneous activity levels. A. The collapse index (CI) of the correlation matrix (filled squares) is found to be larger than that for the covariance matrix (opened squares) across different datasets: f1 to f6: six light-field zebrafish data (10 Hz per volume, this paper); fl: light-sheet zebrafish data (2 Hz per volume, (38)); mn: Neuropixels mouse data (30 Hz downsampled to 10 Hz per volume); mp: two-photon mouse data, (3 Hz per volume, (31)). **B.** The CI as a function of the heterogeneity of neural activity levels ($\mathrm{E}(\sigma^4)$) in simulation and theory, calculated using the Gaussian variational method. We generate ERM where each neuron's activity variance σ_i^2 is i.i.d. sampled from a log-normal distribution with zero mean and a sequence of standard deviation $(0, 0.05, 0.1, \ldots, 0.5)$ in the natural logarithm of the values σ_i^2. We also normalize $\mathrm{E}(\sigma_i^2) = 1$ (Methods). The solid blue line represents the average over 100 ERM realizations, and the shaded area represents SD. The solid red line is the theoretical prediction calculated by the variational method. **C.** Subsampled correlation eigenspectra of a representative example of zebrafish data (fish 1). **D.** Same as **C** but for covariance eigenspectra. **E.** Comparing the pdfs of theoretical spectra (high density and variation method) with finite-size simulations of an intermediate-density ERM. The parameters are $N = 1024$, $\rho = 10.24$, $d = 2$, $L = 10$, $\mu = 0.5$, $\epsilon = 0.03125$, $\sigma_i = 1$. **F.** Same as **E** but with $\rho = 1024$ and $L = 1$. We used 7200 frames of data across all datasets in **A,C,D**.

2.5 Factors not affecting the scale invariance

Having determined the factors that affect the collapse of the subsampled covariance spectra, we next turn our attention to ingredients that have little impact on the scale invariance of the spectrum. First, we find that the shape of the kernel functions $f(\vec{x})$ near $x = 0$ (Fig. S7, table S3) does not affect the distribution of *large eigenvalues* (Fig. 5A). Instead, the distribution of large eigenvalues is determined solely by the tail of $f(x)$ as $x \to \infty$. This further justifies

our use of a specific $f(\vec{x})$ (Eq. (2)).

Second, we explore how the spatial distribution of neurons in the functional space, or *coordinate distribution*, affects the collapse of the eigenspectra. Instead of the uniform distribution in a box used in Eq. (1), we generate neurons from a Gaussian distribution or forming clusters (S1)). In all cases of functional coordinate distributions, the large covariance eigenvalues (that is, the top $1\% \to 50\%$ eigenvalues), with the possible exception of the leading ones, remain the same (Fig. 5B).

Finally, we investigate how the geometry of the functional space affects the covariance spectrum. Specifically, we consider two new cases in which points are uniformly distributed on the surface of a sphere or a hemisphere embedded in $\mathbb{R}^3$. The eigenspectra appear again similar to those of the original ERM model, where the points are uniformly distributed in a 2D box $[0, L]^2$ (Fig. 5C). Taken together, our numerical experiments with modified ERM suggest that our results on the scale invariance of the covariance eigenspectrum in sections 2.2 and 2.4 are robust to various modeling details.

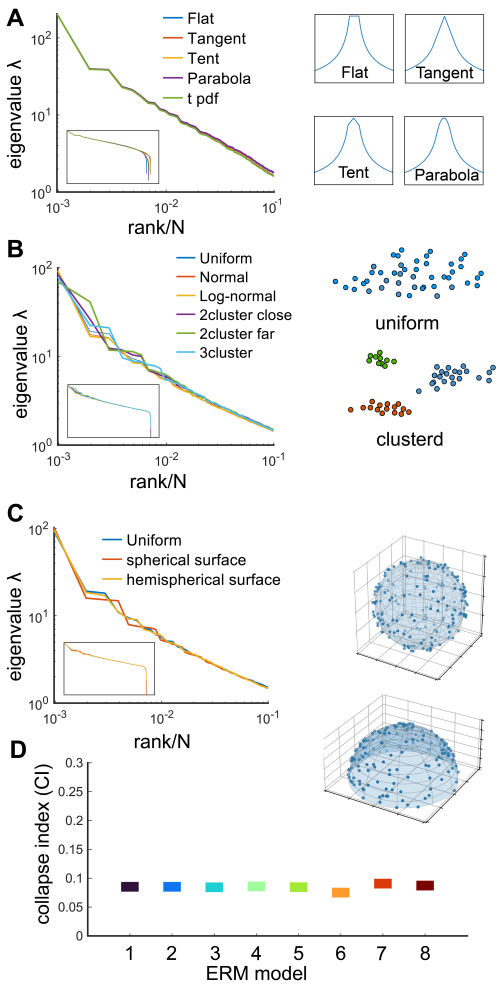

Figure 5. Factors that do not affect the scale invariance. A. Rank plot of the covariance eigenspectrum for ERMs with different $f(\vec{x})$ (see table S3). Diagrams show different slow-decaying kernel functions $f(\vec{x})$ along a 1D slice. **B.** Same as **A** but for different coordinate distributions in the functional space (see text). Diagrams on the right illustrate uniform and clustered coordinate distributions. **C.** Same as **A** but for different geometries of the functional space (see text). Diagrams illustrate spherical and hemispherical surfaces. **D.** CI of the different ERMs considered in A-C. The range on the y-axis is identical to Fig. 4A. On the x-axis, 1: uniform distribution, 2: normal distribution, 3: log-normal distribution, 4: uniform two nearby clusters, 5: uniform two faraway clusters, 6: uniform 3-cluster, 7: spherical surface in $\mathbb{R}^3$, 8: hemispherical surface in $\mathbb{R}^3$. All ERM models in **B**, **C** are adjusted to have a similar distribution of pairwise correlations (Methods).

2.6 Fitting the ERM model to experimental data

Besides being a conceptually simple model to explain the scale invariance in brain-wide activity, the ERM can also be quantitatively applied to the data as a method to analyze and explore the functional structure of neural activity. Our method below consists of two steps, such that we first fit the ERM parameters (d, L, μ, ϵ and σ^2's distribution) and then use the multidimensional scaling (MDS) (40) to infer the functional coordinate $\vec{x}_i$ of neurons.

For a given dimension d and ϵ (recall ϵ being arbitrarily chosen in section 2.2), μ of $f(\vec{x})$ (Eq. (2)), distribution of σ^2 (section 2.2) and ρ (or equivalently L) (section 2.2) can be fitted by comparing the distribution of pairwise correlations in experimental data and ERM (Methods). We found that an embedding dimension $d \leq 5$ gives an overall better fit than $d > 5$ for the experimental pairwise correlation distribution. For simplicity, we use $d = 2$ unless otherwise stated when fitting the kernel function $f(\vec{x})$ and the data covariance matrix.

After determining the parameters of the ERM, we first examine the spectrum of the ERM with uniformly distributed random functional coordinates $\vec{x}_i \in [0, L]^d$. The eigenvalue rank plot (Fig. 6C) has a power-law coefficient $\alpha = 0.55$ that closely matches the experimental $\alpha = 0.47$, suggesting that the key factors described in sections 2.2 and 2.4 are sufficient to recapitulate the experimentally measured covariance spectrum.

Second, we use $f(\vec{x})$ to translate experimental pairwise correlations into pairwise distances for all neurons in the functional space. The embedding coordinates $\vec{x}_i$ in the functional space can then be solved through MDS by minimizing the Sammon error (Methods). The fitted ERM with the embedding coordinates $\vec{x}_i$ and the data variances $\sigma_i^2 = C_{ii}$ reproduces the experimental covariance matrix that includes the cluster structures (Fig. 6D,E) and its subsampling eigenspectra (Fig. 6A,B). The similarity between Fig. 6B and C is also consistent with the notion that specific coordinate distributions in the functional space have little impact on the shape of the eigenspectrum (section 2.5).

Finally, using the embedding coordinates $\vec{x}_i$, we can directly evaluate the similarity between the data $f(\|\vec{x}_i - \vec{x}_j\|)$ and the model $f(\vec{x})$ (Fig. 6F). The matching is close for a wide range of distances, except for small distances and perhaps around the edge of the functional space (see also figures S10 and S11 for plots of all fish datasets). This quantitative similarity to the data confirms our choice to consider a slow-decaying $f(\vec{x})$.

MDS also reveals intriguing clustered structures in the functional space (Fig. 6G, also Fig. S13). This makes us wonder about their corresponding brain regions and potential functional roles in the brain-wide circuit. As a first step, we investigate the relationship between the neural map in the functional space and the anatomical space using the canonical correlation analysis (CCA). In particular, we apply CCA to find a pair of the leading canonical correlation basis vectors $\vec{a}_1$ and $\vec{b}_1$ in the functional space and the anatomical space, respectively (arrows in Fig. 6G,H). These basis vectors satisfy the condition that the projections of the neuron coordinates along them, $\{\vec{x}_i \cdot \vec{a}_1\}$ and $\{\vec{y}_i \cdot \vec{b}_1\}$ ($\vec{y}_i$ is the anatomical coordinate), are maximally correlated among all possible choices of $\vec{a}_1$ and $\vec{b}_1$. Comparison with the neuron-shuffled canonical correlation (Fig. S12) shows that the observed R_{CCA} between the embedding coordinates $\vec{x}_i$ and the anatomical coordinates $\vec{y}_i$ is highly significant. Fig. 6H shows the CCA result for a representative fish (fish 6). In this example, $\vec{b}_1$ is approximately parallel to the rostrocaudal axis. When each neuron i is colored by the projection value $\{\vec{y}_i \cdot \vec{b}_1\}$ and displayed in the *functional space* (Fig. 6G), we observe an interesting correspondence between the clustering structures and the anatomical coordinate (in color). Similarly, we can color each neuron i in the *anatomical space* (Fig. 6H) by the projection value $\{\vec{x}_i \cdot \vec{a}_1\}$, allowing us to observe prominent localizations in brain regions such as the forebrain and the optic tectum. Together, our model reveals the phenomenon that functionally clustered neurons are also anatomically segregated (38). These results are consistent with previous reports, which show that the brain-wide circuit in zebrafish is largely organized along the rostrocaudal axis (42).

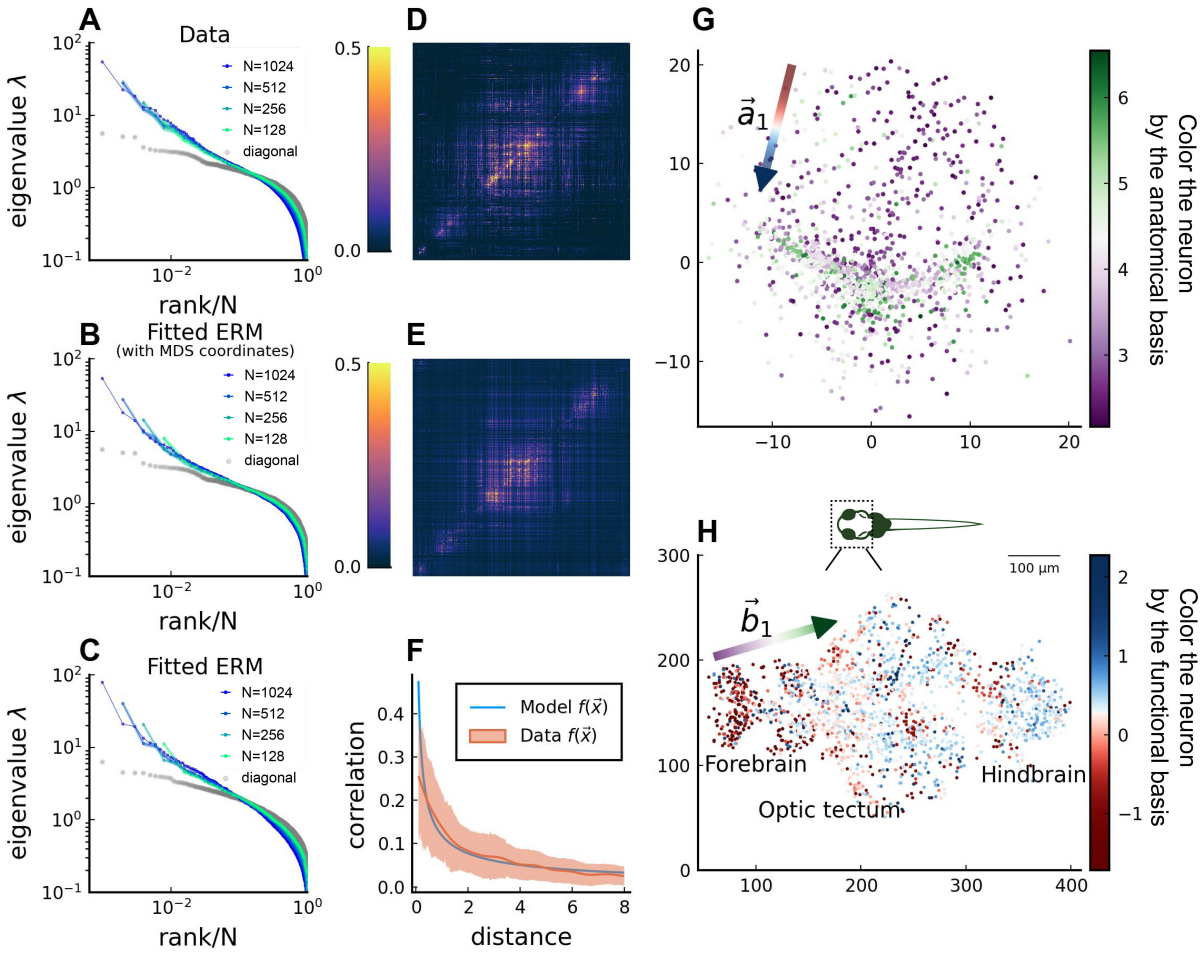

Figure 6. The relationship between the functional and anatomical space by ERM fitting to data. A. Subsampled covariance eigenspectra of the data from fish 6 (number of time frames: 9388). **B.** Subsampled covariance eigenspectra of a fitted ERM model including the MDS coordinates (see text). **C.** Subsampled covariance eigenspectra of a fitted ERM model (see text). **D.** Covariance matrix of the data shown in **A**. **E.** Covariance matrix of the model in **B**. **F.** Comparison of the power-law kernel function $f(\vec{x})$ in the model in **B** (blue line) and the correlation distance relationship in the data (red line). The distance is calculated from the inferred coordinates using MDS. The orange-shaded area shows the SD. **G.** Distribution of neurons in functional space, where each neuron is color-coded by projection of its coordinate along the canonical axis $\vec{b}_1$ in anatomical space (see text). **H.** Distribution of neurons in the anatomical space, where each neuron is color coded by the projection of its coordinate along the canonical axis $\vec{a}_1$ in the functional space (see text).

2.7 Impact of hunting behavior on scale invariance and functional space organization

Last but not least, we examine how the hunting behavior of larval zebrafish (see Fig. 1) shapes the covariance spectrum and the functional organization of brain-wide activity. While our head-fixed animals were unable to capture the prey, they exhibited characteristic eye convergence, that is, both eyes move inward to focus on the central visual field, a behavior commonly associated with the initiation of hunting in larval zebrafish (43, 44). In our experiment, this convergence of the eyes was maintained for a duration of 6.37±4.02 sec (mean±SD, n = 86 convergence events in 5 fish in the hunting essay).

We identify these eye convergence intervals in the co-recorded behavior data and use them as putative labels when the animals are engaged in hunting behavior. When removing these hunting time frames from the Ca^{2+} imaging data to calculate the covariance matrix, we observe that the scale invariance of the eigenspectra still persists (i.e., a similarly small CI is shown in Fig. 4A, Fig. 7). This finding is consistent with observations in other data sets during spontaneous behaviors (Fig. 6A, Fig. S1C-D), suggesting that scale invariance is a general phenomenon in the brain.

Interestingly, the CI for the hunting removed data appears to be significantly lower than in the control case (p-value$= 1.5 \times 10^{-9}$, one-sample t-test, Fig. 7A, B, Fig. S14) that removes the same number of non-hunting time frames (S1). This indicates that engaging in certain behaviors, such as hunting, could actually *reduce* the scale invariance.

Furthermore, in the inferred functional space (similar to Fig. 6G), we observe a prominent reorganization of neurons after the removal of hunting behavior (Fig. 7C-D). This reorganization is evident as neurons in a cluster disperse away from its center of mass (Fig. 7D), resulting in a dramatic decrease in local neuronal density ρ (Eq. (3)). This is quantified by the fold change of the cluster size (i.e., area) (S1 and Fig. 7E). Interestingly, we find a consistent midbrain-hindbrain anatomical distribution for this most dispersed cluster in 4 out of 5 fish (Fig. S15). Our findings suggest that hunting behavior selectively orchestrates neural cell assemblies across a well-defined brain-wide circuit.

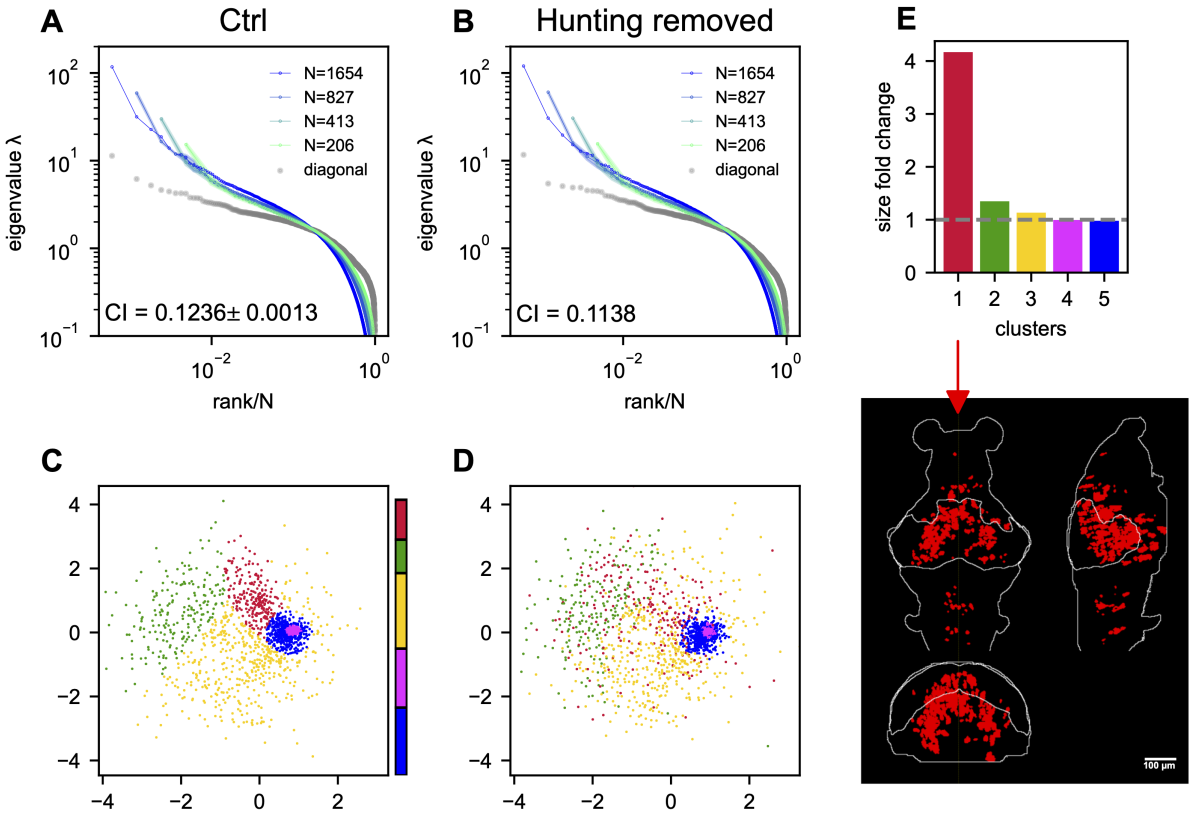

Figure 7. The effects of hunting behavior on scale invariance and functional space organization. A,B. Subsampled covariance eigenspectra of the data from fish 1 calculated from control (**A**) and hunting removed (**B**) data . Ctrl: We randomly remove the same number of non-hunting frames. This process is repeated 10 times, and the mean±SD of the CI is shown in the plot. Hunting removed: The time frames corresponding to the eye-converged intervals (putative hunting state) are removed when calculating the covariance (S1). The CI for the hunting-removed data appears to be statistically smaller than in the control case (p-value$= 1.5 \times 10^{-9}$). **C.** Functional space organization of control data. The neurons are clustered using the Gaussian Mixture Models (GMMs) and their cluster memberships are shown by the color. The color bar represents the proportion of neurons that belong to each cluster. **D.** Similar to **C** but the functional coordinates are inferred from the hunting-removed data. The color code of each neuron is the same as that of the control data (**C**), which allows for a comparison of the changes to the clusters under the hunting-removed condition. **E.** Fold change in size / area (S1) for each cluster (top; the gray dashed line represents a fold change of 1, that is, no change in size) and the anatomical distribution of the most dispersed cluster (bottom).

3 Discussion

In this study, we report that brain-wide neural activity in larval zebrafish is distributed across many dimensions (PCs) with a scale-invariant covariance spectrum. To explain this phenomenon, we use Euclidean Random Matrix (ERM) to model the covariance matrix, where the pairwise correlation is given by a *non-negative* kernel function $f(\vec{x})$ that monotonically decreases with the distance between neurons in the functional space. This nonnegativeness brings about a potential issue when applied to experimental data, where, in fact, a small fraction of pairwise correlations/covariances are negative. We have verified that the spectrum of the data covariance matrix (Fig. S16) remains virtually unchanged when replacing these negative covariances with zero (Fig. S16). This confirms that the ERM remains a good model when the neural dynamics is in a regime where pairwise covariances are mostly positive (45) (see also Fig. 1C, Fig. S1A-D).

There might be concerns regarding the validity of our primary observations due to the finite sampling effect when estimating the data covariance matrix, as well as the limited spatial resolution offered by light field microscopy. We have addressed these potential issues in the following ways (Methods): (1) To ensure comparability between different animals, we maintain an identical number of time samples across all datasets (Fig. 4A). (2) We have verified the sample covariance matrix using datasets with extended recording durations when available (Fig. 6A, Fig. S9A-E). (3) To further validate our conclusions, we have analyzed datasets with single neuron resolution acquired by light-sheet microscopy, two-photon microscopy, and Neuropixels recording (Fig. S1, S1). By taking these steps, our aim is to ensure the robustness and reliability of our findings.

It is also useful to clarify a few potential misconceptions about our analysis. First, our primary objective is to understand why the covariance eigenspectra observed in different datasets and species nearly collapse onto each other upon random subsampling, rather than to explain why the eigenspectra itself follow a power law. Indeed, the experimental data align more closely with the ERM model in the intermediate-density regime $\rho \sim O(1)$, where the power-law eigenspectrum is *only* an approximation for large eigenvalues over a range of 10 folds, consistent with previous observations (32). We show that the eigendensity in this regime (Fig. 4E) deviates significantly from the power law predicted by the high-density theory (Eq. (4)). Nevertheless, the high-density theory offers an expressive and intuitive means to understand this phenomenon.

Second, random subsampling of the neural covariance matrix is not equivalent to subsampling the eigenvalues of a covariance matrix – the latter could trivially result in a collapse of eigenspectra. On the contrary, when we apply random subsampling to the most commonly used covariance matrices in the literature, they do not display the scale-invariant phenomenon (Fig. 3). Thus, our focus is on understanding the unique features and precise conditions that lead to the observed phenomenon.

Third, one of the key factors we identified that contributes to the scale invariance of the covariance spectrum is the slow-decaying kernel function. For the sake of theoretical simplicity, we invoke a power-law kernel function $f(\vec{x}) \sim \|\vec{x}\|^{-\mu}$ to compute the covariance eigenspectrum and examine under what conditions the scale invariance arises. Having a power-law kernel function is *not* a necessary condition for the collapse of the spectrum over subsampling (Fig. S4): those with large scaling coefficient μ (indicating faster decay) in the low-dimensional functional space do not exhibit scale invariance, despite having a decent power law eigenspectrum.

The power-law kernel function is evocative of the spatial correlation function at second-order phase transition in equilibrium statistical mechanics (46). Numerous studies in the literature have investigated the hypothesis of critical brains, suggesting that when the brain is in a critical state, its information processing capabilities are optimized (45, 47, 48). A notable example is the phenomenon of neuronal avalanches – coordinated bursts of activity spanning cell assemblies (47) – which draws an analogy with the sandpile model (49). However, caution should be exercised when drawing such analogies. The brain, like many other biological systems, is open and dissipative. Therefore, the empirical observation of power laws does not necessarily imply that the system has self-organized into a critical state (SOC) (49). This caution is supported by various studies, such as (50).

Returning to our observations, we are not asserting that the spatial correlation function in our data strictly adheres to a power law. The choice of the correlation function in the model is not unique. In fact, when we replace the power-law function with other types of slow-decaying functions, we can still observe a similar collapse of the covariance spectrum upon random subsampling (Fig. S5).

Our research draws inspiration from the recent application of the renormalization group (RG) approach to characterizing the scale invariance of the covariance spectrum (32). Echoing the spirit of Kardanoff's block spin transformation (51), Meshulam et al. (32) devised a distinct procedure to construct size-dependent neuron clusters and their covariance matrices. This was achieved by iteratively identifying the most highly correlated neuron pairs and positioning them adjacently on a lattice with a lattice constant a. As additional neurons were recruited, clusters expanded until the largest cluster approached the system size L (52, 53). Interestingly, when applying this approach to our data, we also observed a similar collapse of the eigenspectra (Fig. S17). In the context of our ERM model, the RG-inspired process can be viewed as a *special* case of sampling where the neuronal density remains fixed at $\rho = 1/a^d$. Consequently, for *any* spatial correlation functions, including power law and exponential (see for example Fig. S18), the covariance eigenspectrum would collapse when this particular procedure is employed to navigate across scales.

In contrast, the subsampling procedure we consider results in a change in ρ, thus demanding more rigorous conditions to achieve a scale-invariant covariance spectrum. This approach is also simpler and can be related to situations naturally occurring in a wide range of experimental data, such as multi-electrode recordings.

When fitting the eigenvalue rank plot using a power-law function, we find that the eigenspectrum decays with a coefficient $\alpha < 1$. Interestingly, Stringer et al. (33) discovered that in the mouse visual cortex, the neural covariance spectrum in the stimulus space exhibited a power law that decayed faster with $\alpha > 1$; theoretical analysis (33) suggests that $\alpha > 1$ is a mathematical necessity for a smooth and differentiable population code. These two observations are not contradictory since they (33) examined the signal correlation, that is, the correlation of neural responses to visual stimuli, by excluding trial-to-trial variability, while our covariance is calculated from single-trial activity closer to the noise correlation (54). Furthermore, the neural activity space representing spontaneous and behavior-related activity and the subspace encoding sensory stimuli can be orthogonal to each other (31), and the corresponding eigenspectra can have very different statistical properties.

A less studied but important factor that improves the collapse of the covariance spectrum is the heterogeneity of neural activity levels (quantified by variance σ_i^2 here). For simplicity, we assume that the variances in neural activity $\{\sigma_i^2\}, i = 1, 2, \ldots, N$, are drawn independently in our ERM model (Eq. (1)). To verify this assumption, we compare the CI of the original dataset with that of the variance-shuffled data, in which σ_i^2 for different neurons are randomly permuted, while the correlations remain the same (this will also modify the covariances $C_{i \neq j}$ according to Eq. (1)). In 4 out of 6 the light-field fish dataset (f1-f6), 1 out of 3 the light-sheet imaging fish datasets, 0 out of 3 the Neuropixels datasets, and 1 out of 3 the two-photon calcium imaging datasets, the CIs of the original and shuffled data are not significantly different, supporting the independence assumption (Fig. S6C). In the other datasets, however, the CI of the original data is significantly smaller than that of the shuffled data ($< 2.5\%$-quantile), indicating that there are additional fine statistical structures that *further improve* the scale invariance of the eigenspectrum. Incorporation of these additional covariance structures into the model and the characterization of their effect on the eigenspectrum will be considered in future studies.

An interesting question, which connects to other lines of research (34, 55), is how the geometry of the functional space/manifold affects the covariance eigenspectrum. With numerical simulations, we find that the geometry of the functional space does not necessarily affect the spectrum and its scale invariance (Fig. 5). Nevertheless, it is not fully conclusive therefore requires further study in that we cannot explore all possible topologies of the functional space. Complementary methods, such as the calculation of persistent homology (56), may provide new insight into the topological structure of the functional space. Interestingly, a case of spherical functional space is closely related to a recent model developed by Morrell et al. (34), which successfully replicated the scale-invariance phenomenon observed in (32). In this model, neurons are driven by m latent variables with random readout vectors. If we focus on the spatial aspects of neural activity, the model can be approximately viewed as a generalized ERM (57) on a sphere in $\mathbb{R}^{m-1}$ (S3). This connection between the two models means that the dimension of the functional space, which contributes to the scale invariance, may also be interpreted as the number of globally projecting latent variables.

Finally, we show how to fit the ERM to the experimental data and infer functional coordinates using MDS. This approach allows quantitative exploration of the relationship between functional space and anatomical space in the brain (Fig. 6). In particular, we found that hunting behavior reorganizes neurons in the functional space (Fig. 7). An interesting avenue for future research would be to extend this approach to compare behavior states on multiple timescales (27, 42, 58) or between healthy and diseased subjects.

4 Methods

4.1 Covariance matrix and subsampled eigenspectrum

To begin, we multiplied the inferred firing rate of each neuron (see S1) by a constant such that in the resulting activity trace x_i, the mean of x_i *over the nonzero frames* is equal to one (32). Consistent with the literature (32), this step aims to eliminate possible confounding factors in the raw activity traces, such as the heterogeneous expression level of the fluorescence protein within neurons and the non-linear conversion of the electrical signal to Ca^{2+} concentration. Note that after this scaling, neurons can still have different activity levels characterized by the variance of x_i, due to differences in the sparsity of activity (proportion of nonzero frames) and the distribution of nonzero x_i values. For consistency, we used the same number of time frames $T = 7,200$ when comparing CI across all the datasets (Fig. 4, Fig. S6). For other cases (Fig. 1, Fig. 6, Fig. 7, Fig. S1, figures S10, S11, S13, S14 and S16), we analyzed the full length of the data (number of time frames: fish 1 - 7495, fish 2 - 9774, fish 3 - 13904, fish 4 - 7318, fish 5 - 7200, fish 6 - 9388). Next, the covariance matrix was calculated as

Notation	Description
C	covariance matrix, Eq. (1)
C_{ij}	pairwise covariance between neuron i, j; entries of C
λ	eigenvalue of covariance matrix
$p(\lambda)$	probability density function of covariance eigenvalue, Eq. (3)
r	rank of an eigenvalue in descending order, Eq. (4)
q	fraction of eigenvalues up to λ and $q = r/N$, Eq. (5)
$f(\vec{x}) = f(\lVert\vec{x}_i - \vec{x}_j\rVert)$	kernel function or distance-correlation function, Eq. (2)
$\tilde{f}(\vec{k})$	Fourier transform of $f(\vec{x})$, $\tilde{f}(\vec{k}) = \int_{\mathbb{R}^d} f(\vec{x}) e^{-i\vec{x}\cdot\vec{k}} \mathrm{d}^d\vec{x}$
μ	power-law exponent in $f(\vec{x})$, Eq. (2)
ϵ	parameter in $f(\vec{x})$ to smooth the singularity near 0, Eq. (2)
N	number of neurons
L	linear box size of the functional space
ρ	density of neurons in the functional space
d	dimension of the functional space
σ_i^2	variance of neural activity, Eq. (2)
α	power-law coefficient of eigenspectrum in the rank plot, section 2.1
$\vec{x}_i$	neuron i's coordinate in functional space
$\vec{y}_i$	neuron i's coordinate in anatomical space
$\vec{a}_1$	leading canonical correlation basis vector in the functional space, section 2.6
$\vec{b}_1$	leading canonical correlation basis vector in the anatomical space, section 2.6
R_{CCA}	the first canonical correlation, section 2.6

Table 1. Table of notations.

$C_{ij} = \frac{1}{T-1}\sum_{t=1}^{T}(x_i(t) - \bar{x}_i)(x_j(t) - \bar{x}_j)$, where $\bar{x}_i$ is the mean of x_i over time. Finally, to visualize covariance matrices on a common scale, we multiplied matrix C by a constant such that the average of its diagonal entries is equal to one, that is, $\mathrm{Tr}(C)/N = 1$. This scaling does not alter the distribution of covariance eigenvalues, but sets their mean at 1 (see Eq. (3), section 2.2).

We used an iterative procedure to subsample the covariance matrix C (calculated from data or as simulated ERMs). To maintain consistency across datasets, we randomly chose $N_0 = 1{,}024$ neurons from each zebrafish dataset as the initial set of neurons (the remainder remain fixed for all analyses). In the first iteration, we randomly select half of the neurons. The covariance matrix for these selected neurons is a $\frac{N}{2} \times \frac{N}{2}$ diagonal block of C. Similarly, the covariance matrix of the unselected neurons is another diagonal block of the same size. In the next iteration, we similarly create two new subsampled blocks with half the number of neurons for each of the blocks we currently have. Repeating this process for n iterations results in 2^n blocks, each containing $N := N_0/2^n$ neurons.

At each iteration, the eigenvalues of each block were calculated and averaged after they were sorted in descending order. Finally, the averaged eigenvalues were plotted against rank/N on a log-log scale. To numerically compute the eigenvalue probability density function in our model, we generated ERM 100 times, each of which was subsampled using the method described above.

To determine the overall power-law coefficient of the eigenspectra, α, throughout subsampling, we fitted a straight line in the log-log rank plot to the large eigenvalues that combined the original and three iterations of subsampled covariance matrices (selecting the top 10% eigenvalues for each matrix and excluding the first four largest ones for each matrix). We averaged the estimated α over 10 repetitions of the entire subsampling procedure. R^2 of the power-law fit was computed in a similar way.

To visualize the statistical structures of the original and subsampled covariance matrices, the orders of the neurons (i.e. columns and rows) are determined by the following algorithm. We first construct a symmetric Toeplitz matrix $\mathcal{T}$, with entries $\mathcal{T}_{i,j} = t_{i-j}$ and $t_{i-j} \equiv t_{j-i}$. The vector $\vec{t} = [t_0, t_1, \ldots, t_{N-1}]$ is equal to the mean covariance vector of each neuron calculated below. Let $\vec{c_i}$ be a row vector of the data covariance matrix; we identify $\vec{t} = \frac{1}{N}\sum_{i=1}^{N} D(\vec{c_i})$, where $D(\cdot)$ denotes a numerical ordering operator, namely rearrange the elements in a vector $\vec{c}$ such that $c_0 \geq c_1 \geq \ldots \geq c_{N-1}$. The second step was to find a permutation matrix P such that $\|\mathcal{T} - PCP^T\|_F$ is minimized, where $\| \, \|_F$ denotes the Frobenius norm. This quadratic assignment problem was solved by simulated annealing. Note that after subsampling, the smaller matrix will appear different from the larger one. We need to perform the above reordering algorithm for every subsampled matrix so that matrices of different sizes become similar in Fig. 1F.

The composite covariance matrix with substituted eigenvectors in (Fig. 1H) was created as described in the following steps. First, we generated a random orthogonal matrix U_r (based on the Haar measure) for the new eigenvectors. This was achieved by QR decomposition $A = U_r R$ of a random matrix A with i.i.d. entries $A_{ij} \sim \mathcal{N}(0, 1/N)$. The composite covariance matrix C_r was then defined as $C_r := U_r \Lambda U_r^T$, where Λ is a diagonal matrix that contains the eigenvalues of C. Note that since all the eigenvalues are real and U_r is orthogonal, the resulting C_r is a real and symmetric matrix. By construction, C_r and C have the same eigenvalues, but their *subsampled* eigenspectra can differ.

4.2 ERM model

We consider the eigenvalue distribution or spectrum of the matrix C at the limit of $N \gg 1$ and $L \gg 1$. This spectrum can be analytically calculated in both high-density ($\rho \gg 1$) and intermediate-density ($\rho = O(1)$) scenarios using the replica method (39). The following sketch shows our approach, and detailed derivations can be found in S3. To calculate the probability density function of the eigenvalues (or eigendensity), we first compute the resolvent or Stieltjes transform $g(z) = -\frac{2}{N}\partial_z \left\langle \ln \det(zI - C)^{-1/2} \right\rangle$, $z \in \mathbb{C}$. Here $\langle ... \rangle$ is the average across the realizations of C (that is, random $\vec{x}_i$' s and σ_i^2' s). The relationship between the resolvent and the eigendensity is given by the Sokhotski-Plemelj formula:

$$p(\lambda) = -\frac{1}{\pi} \lim_{\eta \to 0^+} \mathbf{Im}\, g(\lambda + i\eta), \tag{6}$$

where $\mathbf{Im}$ means imaginary part.

Here we follow the field-theoretic approach (39), which turns the problem of calculating the resolvent to a calculation of the partition function in statistical physics by using the replica method. In the limit $N \to \infty$, $L^d \to \infty$, ρ being finite, by performing a leading order expansion of the canonical partition function at large z (S3), we find the resolvent is given by

$$g(z) = \frac{1}{\rho} \int \frac{\mathrm{d}^d \vec{k}}{(2\pi)^d} \frac{1}{z - \rho E(\sigma^2) \tilde{f}(\vec{k})} \tag{7}$$

the eigendensity for $\rho \gg 1$ (Eq. (3)) can be derived from equations (6) and (7).

In the intermediate density $\rho = O(1)$, an improved approximation can be derived using the Gaussian variational method (39). Unlike the high-density theory where the eigendensity has an explicit expression, here the resolvent $g(z)$ no longer has an explicit expression and is given by the following equation

$$g(z) = \left\langle \frac{1}{z - \sigma^2 \int \mathrm{D}\vec{k}\, \tilde{G}(\vec{k}, z)} \right\rangle_\sigma, \tag{8}$$

where $\langle ... \rangle_\sigma$ computes the expectation value of the term within the bracket with respect to σ, namely $\langle ... \rangle_\sigma \equiv \int ... p(\sigma) \mathrm{d}\sigma$. Here and in the following, we denote $\int \mathrm{D}\vec{k} \equiv \int \frac{\mathrm{d}^d \vec{k}}{(2\pi)^d}$. The function $G(\vec{k}, z)$ is determined by a self-consistent equation,

$$\frac{1}{\tilde{f}(\vec{k})} = \frac{1}{\tilde{G}(\vec{k}, z)} + \left\langle \frac{\rho\sigma^2}{z - \sigma^2 \int \mathrm{D}\vec{k}\, \tilde{G}(\vec{k}, z)} \right\rangle_\sigma \tag{9}$$

We can solve $\int \mathrm{D}\vec{k}\, G(\vec{k}, z)$ from Eq. (9) numerically and below is an outline and the details are explained in S3. Let us define the integral $\mathcal{G} \equiv \int \mathrm{D}\vec{k}\, \tilde{G}(\vec{k}, z)$. First, we substitute $z \equiv \lambda + i\eta$ into Eq. (9) and write $\mathcal{G} = \mathbf{Re}\mathcal{G} + i\mathbf{Im}\mathcal{G}$. Eq. (9) can thus be decomposed into its real part and imaginary part, and a set of nonlinear and integral equations, each of which involves both $\mathbf{Re}\mathcal{G}$ and $\mathbf{Im}\mathcal{G}$. We solve these equations at the limit $\eta \to 0$ using a fixed-point iteration that alternates between updating $\mathbf{Re}\mathcal{G}$ and $\mathbf{Im}\mathcal{G}$ until convergence.

We find that the variational approximations exhibit excellent agreement with the numerical simulation for both large and intermediate ρ (for $\rho = 256$ and $\rho = 10.24$, Fig. 4E,F). To further elucidate the connection between the two different methods, we estimate the condition when the result of high-density theory (Eq. (3)) matches that of the variational method (equations (8) and (9)) (S3).

Throughout the paper, we have mainly considered the particular kernel function $f(\vec{x}) = \epsilon^\mu (\epsilon^2 + \|x\|^2)^{-\mu/2}$ (Eq. (2), Fig. 2A, B). This approximate power-law $f(\vec{x})$ has the advantage of having an analytical expression for its Fourier transform, which is crucial for the high-density theory (Eq. (3)),

$$\tilde{f}(\vec{k}) = \frac{2^{\frac{d-\mu+2}{2}} \pi^{\frac{d}{2}} k^{\frac{\mu-d}{2}} \epsilon^{\frac{\mu+d}{2}} K_{(d-\mu)/2}(k\epsilon)}{\Gamma(\mu/2)}, \quad k = \|\vec{k}\| \tag{10}$$

Here $K_\alpha(x)$ is the modified Bessel function of the second kind, and $\Gamma(x)$ is the Gamma function. We calculated the above formulas analytically for $d = 1, 2, 3$ with the assistance of Mathematica and conjectured the case for general dimension d, which we confirmed numerically for $d \leq 10$.

We want to explain two technical points relevant to the interpretation of our numerical results and the choice of $f(\vec{x})$. Unlike the case in the usual ERM, here we allow $f(\vec{x})$ to be non-integrable (over $\mathbb{R}^d$), which is crucial to allow power law $f(\vec{x})$. The nonintegrability violates a condition in the classical convergence results of the ERM spectrum (59) as $N \to \infty$. We believe that this is exactly the reason for the departure of the first few eigenvalues from our theoretical spectrum (e.g., in Fig. 2). Our hypothesis is also supported by ERM simulations with integrable $f(\vec{x})$ (Fig. S3), where the numerical eigenspectrum matches closely with our theoretical one, including the leading eigenvalues. For ERM to be a legitimate model for covariance matrices, we need to ensure that the resulting matrix C is positive semidefinite. According to the Bochner theorem (60), this is equivalent to the Fourier transform (FT) of the kernel function $\tilde{f}(\vec{k})$ being nonnegative for all frequencies. For example, in 1D, a rectangle function $\mathrm{rect}(x) = \begin{cases} 1, & \text{if } |x| \leq \frac{1}{2} \\ 0, & \text{otherwise} \end{cases}$ does not meet the condition (its FT is $\mathrm{sinc}(x) = \frac{\sin(x)}{x}$), but a tent function $\mathrm{tent}(x) = \begin{cases} 1 - |x|, & \text{if } |x| \leq 1 \\ 0, & \text{otherwise} \end{cases}$ does (its FT is $\mathrm{sinc}^2(x)$). For the particular kernel function $f(\vec{x})$ in Eq. (2), this condition can be easily verified using the analytical expressions of its Fourier transform (Eq. (10)). The integral expression for $K_\alpha(x)$, given as $K_\alpha(x) = \int_0^\infty e^{-x \cosh t} \cosh(\alpha t) dt$, shows that $K_\alpha(x)$ is positive for all $x > 0$. Likewise, the Gamma function $\Gamma(x) > 0$. Therefore, the Fourier transform of Eq. (2) is positive and the resulting matrix C (of any size and values of $\vec{x}_i$) is guaranteed to be positive definite.

4.3 Fitting ERM to data

4.3.1 Estimating the ERM parameters. Our ERM model has 4 parameters: μ, and ϵ dictates the kernel function $f(\vec{x})$, whereas the box size L and the embedding dimension d determine the neuronal density ρ. In the following, we describe an approximate method to estimate these parameters from pairwise correlations measured experimentally $R_{ij} = \frac{C_{ij}}{\sigma_i \sigma_j}$. We proceed by deriving a relationship between the correlation probability density distribution $h(R)$ and the pairwise distance probability density distribution $g(u) := g(\|\vec{x}_1 - \vec{x}_2\|)$ in the functional space, from which the parameters of the ERM can be estimated.

Consider a distribution of neurons in the functional space with a coordinate distribution $p(\vec{x})$. The pairwise

distance density function $g(u)$ is related to the spatial point density by the following formula:

$$g(u) = \int p(\vec{x}_1)p(\vec{x}_2)\delta(\|\vec{x}_1 - \vec{x}_2\| - u)\mathrm{d}\vec{x}_1\mathrm{d}\vec{x}_2 \tag{11}$$

In the case of uniform distribution, $p(\vec{x}_1) = p(\vec{x}_2) = 1/V = 1/L^d$. For other spatial distributions, Eq. (11) cannot be explicitly evaluated. We therefore make a similar approximation by focusing on a small pairwise distance (i.e., large correlation):

$$p(\vec{x}_1) \approx p(\vec{x}_2) \approx p(\frac{\vec{x}_1 + \vec{x}_2}{2}) \tag{12}$$

By a change of variables:

$$\vec{X} = \frac{\vec{x}_1 + \vec{x}_2}{2}, \;\; \vec{u} = \vec{x}_1 - \vec{x}_2,$$

Eq. (11) can be rewritten as

$$g(u) \approx \int p^2(\vec{X})\delta(\|\vec{u}\| - u)\mathrm{d}\vec{X}\mathrm{d}\vec{u} = S_{d-1}(u)\int p^2(\vec{X})\mathrm{d}\vec{X} \tag{13}$$

where $S_{d-1}(u)$ is the surface area of $d-1$ sphere with radius u.

With the approximate power-law kernel function $R = f(u) \approx (\frac{\epsilon}{u})^\mu$, the probability density function of pairwise correlation $h(R)$ is given by:

$$h(R) = g(u)\left|\frac{\mathrm{d}u}{\mathrm{d}R}\right| = \frac{2\pi^{\frac{d}{2}}\epsilon^d}{\Gamma(\frac{d}{2})\mu R^{(\mu+d)/\mu}}\int p^2(\vec{X})\mathrm{d}\vec{X} \tag{14}$$

Taking the logarithm on both sides

$$\log h(R) = \log\left(\epsilon^d \int p^2(\vec{X})\mathrm{d}\vec{X}\right) + \log\frac{2\pi^{\frac{d}{2}}}{\Gamma(\frac{d}{2})\mu} - \frac{\mu+d}{\mu}\log R \tag{15}$$

Eq. (15) is the key formula for ERM parameter estimate. In the case of a uniform spatial distribution, $\epsilon^d\int p^2(\vec{X})\mathrm{d}\vec{X} = \epsilon^d/V = (\epsilon/L)^d$. For a given d, we can therefore estimate μ and $(\epsilon/L)^d$ separately by fitting $h(R)$ on the log-log scale using the linear least squares.

Note that ϵ and L are a pair of redundant parameters: once ϵ is given, L is also determined. We set $\epsilon = 0.03125$ throughout the article. Furthermore, knowing $(\epsilon/L)^d$ enables us to determine *a fundamental dimensionless parameter*

$$\rho\epsilon^d := N(\epsilon/L)^d,$$

which tells us whether the experimental data are better described by the high-density theory or the Gaussian variational method (S3). Indeed, the fitted $\rho\epsilon^d \sim 10^{-3} - 10^0$ is much smaller than 1, consistent with our earlier conclusion that neural data are better described by an ERM model in the intermediate-density regime.

Notably, we found that a smaller embedding dimension $d \leq 5$ gave a better fit to the overall pairwise correlation distribution. The following is an empirical explanation. As d grows, to best fit the slope of $\log h(R) - \log R$, μ will also grow. However, for very high dimensions d, the y intercept would become very negative, or equivalently, the fitted correlation would become extremely small. This can be verified by examining the leading order $\log R$ independent term in Eq. (15), which can be approximated as $d\log\frac{\epsilon}{L} + \frac{d}{2}\left(\log\pi + 1 - \log\frac{d}{2}\right)$. It becomes very negative for large d since $\epsilon \ll L$ by construction. Throughout this article, we use $d = 2$ when fitting the experimental data with our ERM model.

The above calculation can be extended to the cases where the coordinate distribution $p(\vec{x})$ becomes dependent on other parameters. To estimate the parameters in coordinate distributions that can generate ERMs with a similar pairwise correlation distribution (Fig. 5), we fixed the integral value $\int p^2(\vec{x})\mathrm{d}\vec{x}$. Consider, for example, a transformation of the uniform coordinate distribution to the normal distribution $\mathcal{N}(\mu_p = 0, \sigma_p^2\mathbf{I})$ in $\mathbb{R}^2$. We imposed $\int p^2(\vec{x})\mathrm{d}\vec{x} = 1/(4\pi\sigma_p^2) = 1/L^2$. For the log-normal distribution, a similar calculation led to $L\exp(\sigma_p^2/4 - \mu_p) = 2\sqrt{\pi}\sigma_p$. The numerical values for these parameters are shown in S1. However, note that due

to the approximation we used (Eq. (12)), our estimate of the ERM parameters becomes less accurate if the density function $p(\vec{x})$ changes rapidly over a short distance in the functional space. More sophisticated methods, such as grid search, may be needed to tackle such a scenario.

Lastly, we fit the distribution of σ^2 (the diagonal entries of the covariance matrix C) to a log-normal distribution by estimating the maximum likelihood.

4.3.2 Multidimensional Scaling (MDS). With the estimated ERM parameters (μ in $f(\vec{x})$ and the box size L for given ϵ and d, see section 4.3.1), we performed MDS to infer neuronal coordinates $\vec{x}_i$ in functional space. First, we computed a pairwise correlation $R_{ij} = \frac{C_{ij}}{\sigma_i \sigma_j}$ from the data covariances. Next, we calculated the pairwise distance, denoted by u^*_{ij}, by computing the inverse function of $f(\vec{x})$ with respect to the absolute value of R_{ij}, $u^*_{ij} = f^{-1}(|R_{ij}|)$. We used the absolute value $|R_{ij}|$ instead of R_{ij} as a small percentage of R_{ij} are negative (Fig. 1C) where the distance is undefined. This substitution by the absolute value serves as a simple workaround for the issue and is only used here in the analysis to infer the neuronal coordinates by MDS. Finally, we estimated the embedding coordinates $\vec{x}_i$ for each neuron by the SMACOF algorithm (Scaling by MAjorizing a COmplicated Function (61)), which minimizes the Sammon error

$$E = \frac{1}{\sum\limits_{i<j} u^*_{ij}} \sum_{i<j} \frac{(u^*_{ij} - u_{ij})^2}{u^*_{ij}} \tag{16}$$

where $u_{ij} = \|\vec{x}_i - \vec{x}_j\|$ is the pairwise distance in the embedding space calculated above.

To reduce errors at large distances (i.e., small correlations with $R_{ij} < f(L)$, where L is estimated box size), we performed a soft cut-off at a large distance:

$$\begin{aligned} u^*_{ij} &= f^{-1}(|R_{ij}|), & R_{ij} \geq f(L) \\ u^*_{ij} &= L \log(f^{-1}(|R_{ij}|)/L) + L, & R_{ij} < f(L) \end{aligned} \tag{17}$$

During the optimization process, we started at the embedding coordinates estimated by the classical MDS (40), with an initial sum of squares distance error that can be calculated directly, and ended with an error or its gradient smaller than 10^{-4}.

4.4 Canonical-Correlation Analysis (CCA)

Here we briefly explain the CCA method (62) for completeness. The basis vectors $\vec{a}_1$ and $\vec{b}_1$, in the functional and anatomical space, respectively, were found by maximizing the correlation $R_{CCA} = corr(\{\vec{a}_1 \cdot \vec{x}_i\}, \{\vec{b}_1 \cdot \vec{y}_i\})$. Here $\{\vec{x}_i\}$, $\{\vec{y}_i\}$ represent the coordinates in functional and anatomical spaces, respectively. The resulting maximum correlation is R_{CCA} . To check the significance of the canonical correlation, we shuffled the functional space coordinates $\{\vec{x}_i\}$ across neurons' identity and re-calculated the canonical correlation with the anatomical coordinates, as shown in Fig. 6F.

Code and data availability

The source code and data used to produce all the figures will be available upon publication.

Supplementary information

S1 Supplementary Methods. S1 comprises additional details of the Materials and Methods.
S2 Supplementary figures and table. S2 comprises 18 supplementary figures and 1 supplementary table.
S3 Supplementary text S3 includes additional details of the theoretical calculations and 3 supplementary figures.

Reference

1. Cunningham, J. P. and Yu, B. M. Dimensionality reduction for large-scale neural recordings. *Nature Neuroscience*, 17(11): 1500–1509, Nov. 2014. doi: $10.1038/\mathrm{nn}.3776$.
2. Williamson, R. C., Doiron, B., Smith, M. A., and Yu, B. M. Bridging large-scale neuronal recordings and large-scale network models using dimensionality reduction. *Current Opinion in Neurobiology*, 55:40–47, Apr. 2019. doi: $10.1016/\mathrm{j.conb}.2018.12.009$.
3. Schneidman, E., Berry, M. J., Segev, R., and Bialek, W. Weak pairwise correlations imply strongly correlated network states in a neural population. *Nature*, 440(7087):1007–1012, Apr. 2006. doi: $10.1038/\mathrm{nature}04701$.

4. Mazor, O. and Laurent, G. Transient Dynamics versus Fixed Points in Odor Representations by Locust Antennal Lobe Projection Neurons. *Neuron*, 48(4):661–673, Nov. 2005. doi: 10.1016/j.neuron.2005.09.032.
5. Si, G., Kanwal, J. K., Hu, Y., Tabone, C. J., Baron, J., Berck, M., Vignoud, G., and Samuel, A. D. Structured Odorant Response Patterns across a Complete Olfactory Receptor Neuron Population. *Neuron*, 101(5):950–962.e7, Mar. 2019. doi: 10.1016/j.neuron.2018.12.030.
6. Briggman, K. L., Abarbanel, H. D. I., and Kristan, W. B. Optical Imaging of Neuronal Populations During Decision-Making. *Science*, 307(5711):896–901, Feb. 2005. doi: 10.1126/science.1103736.
7. Mante, V., Sussillo, D., Shenoy, K. V., and Newsome, W. T. Context-dependent computation by recurrent dynamics in prefrontal cortex. *Nature*, 503(7474):78–84, Nov. 2013. doi: 10.1038/nature12742.
8. Yang, W., Tipparaju, S. L., Chen, G., and Li, N. Thalamus-driven functional populations in frontal cortex support decision-making. *Nature Neuroscience*, 25(10):1339–1352, Oct. 2022. doi: 10.1038/s41593-022-01171-w.
9. Churchland, M. M., Cunningham, J. P., Kaufman, M. T., Foster, J. D., Nuyujukian, P., Ryu, S. I., and Shenoy, K. V. Neural population dynamics during reaching. *Nature*, 487(7405):51–56, July 2012. doi: 10.1038/nature11129.
10. Lindén, H., Petersen, P. C., Vestergaard, M., and Berg, R. W. Movement is governed by rotational neural dynamics in spinal motor networks. *Nature*, 610(7932):526–531, Oct. 2022. doi: 10.1038/s41586-022-05293-w.
11. Urai, A. E., Doiron, B., Leifer, A. M., and Churchland, A. K. Large-scale neural recordings call for new insights to link brain and behavior. *Nature Neuroscience*, 25(1):11–19, Jan. 2022. doi: 10.1038/s41593-021-00980-9. Number: 1 Publisher: Nature Publishing Group.
12. Shadlen, M. N. and Newsome, W. T. The Variable Discharge of Cortical Neurons: Implications for Connectivity, Computation, and Information Coding. *Journal of Neuroscience*, 18(10):3870–3896, May 1998. doi: 10.1523/JNEUROSCI.18-10-03870.1998.
13. Pernice, V., Staude, B., Cardanobile, S., and Rotter, S. How Structure Determines Correlations in Neuronal Networks. *PLoS Computational Biology*, 7(5):e1002059, May 2011. doi: 10.1371/journal.pcbi.1002059.
14. Kohn, A., Coen-Cagli, R., Kanitscheider, I., and Pouget, A. Correlations and Neuronal Population Information. *Annual Review of Neuroscience*, 39(1):237–256, 2016. doi: 10.1146/annurev-neuro-070815-013851. _eprint: https://doi.org/10.1146/annurev-neuro-070815-013851.
15. Cayco-Gajic, N. A., Zylberberg, J., and Shea-Brown, E. Triplet correlations among similarly tuned cells impact population coding. *Frontiers in Computational Neuroscience*, 9, 2015.
16. Yoon, H. and Sompolinsky, H. The Effect of Correlations on the Fisher Information of Population Codes. In *Advances in Neural Information Processing Systems*, volume 11. MIT Press, 1998. URL https://proceedings.neurips.cc/paper/1998/hash/41a60377ba920919939d83326ebee5a1-Abstract.html.
17. Moreno-Bote, R., Beck, J., Kanitscheider, I., Pitkow, X., Latham, P., and Pouget, A. Information-limiting correlations. *Nature Neuroscience*, 17(10):1410–1417, Oct. 2014. doi: 10.1038/nn.3807.
18. Franke, F., Fiscella, M., Sevelev, M., Roska, B., Hierlemann, A., and Azeredo da Silveira, R. Structures of Neural Correlation and How They Favor Coding. *Neuron*, 89(2):409–422, Jan. 2016. doi: 10.1016/j.neuron.2015.12.037.
19. Azeredo da Silveira, R. and Rieke, F. The Geometry of Information Coding in Correlated Neural Populations. *Annual Review of Neuroscience*, 44(1):403–424, 2021. doi: 10.1146/annurev-neuro-120320-082744.
20. Panzeri, S., Moroni, M., Safaai, H., and Harvey, C. D. The structures and functions of correlations in neural population codes. *Nature Reviews Neuroscience*, 23(9):551–567, Sept. 2022. doi: 10.1038/s41583-022-00606-4.
21. Song, S., Miller, K. D., and Abbott, L. F. Competitive Hebbian learning through spike-timing-dependent synaptic plasticity. *Nature Neuroscience*, 3(9):919–926, Sept. 2000. doi: 10.1038/78829.
22. Kanashiro, T., Ocker, G. K., Cohen, M. R., and Doiron, B. Attentional modulation of neuronal variability in circuit models of cortex. *eLife*, 6:e23978, June 2017. doi: 10.7554/eLife.23978.
23. Rosenbaum, R., Smith, M. A., Kohn, A., Rubin, J. E., and Doiron, B. The spatial structure of correlated neuronal variability. *Nature Neuroscience*, 20(1):107–114, Jan. 2017. doi: 10.1038/nn.4433.
24. Huang, C., Ruff, D. A., Pyle, R., Rosenbaum, R., Cohen, M. R., and Doiron, B. Circuit Models of Low-Dimensional Shared Variability in Cortical Networks. *Neuron*, 101(2):337–348.e4, Jan. 2019. doi: 10.1016/j.neuron.2018.11.034.
25. Sadtler, P. T., Quick, K. M., Golub, M. D., Chase, S. M., Ryu, S. I., Tyler-Kabara, E. C., Yu, B. M., and Batista, A. P. Neural constraints on learning. *Nature*, 512(7515):423–426, Aug. 2014. doi: 10.1038/nature13665.
26. Gallego, J. A., Perich, M. G., Naufel, S. N., Ethier, C., Solla, S. A., and Miller, L. E. Cortical population activity within a preserved neural manifold underlies multiple motor behaviors. *Nature Communications*, 9(1):4233, Oct. 2018. doi: 10.1038/s41467-018-06560-z.
27. Kaplan, H. S. and Zimmer, M. Brain-wide representations of ongoing behavior: a universal principle? *Current Opinion in Neurobiology*, 64:60–69, Oct. 2020. doi: 10.1016/j.conb.2020.02.008.
28. Hallinen, K. M., Dempsey, R., Scholz, M., Yu, X., Linder, A., Randi, F., Sharma, A. K., Shaevitz, J. W., and Leifer, A. M. Decoding locomotion from population neural activity in moving C. elegans. *eLife*, 10:e66135, July 2021. doi: 10.7554/eLife.66135.
29. Schaffer, E. S., Mishra, N., Whiteway, M. R., Li, W., Vancura, M. B., Freedman, J., Patel, K. B., Voleti, V., Paninski, L., Hillman, E. M. C., Abbott, L. F., and Axel, R. Flygenvectors: The spatial and temporal structure of neural activity across the fly brain, Sept. 2021. URL https://www.biorxiv.org/content/10.1101/2021.09.25.461804v1.
30. Musall, S., Kaufman, M. T., Juavinett, A. L., Gluf, S., and Churchland, A. K. Single-trial neural dynamics are dominated by richly varied movements. *Nature Neuroscience*, 22(10):1677–1686, Oct. 2019. doi: 10.1038/s41593-019-0502-4.
31. Stringer, C., Pachitariu, M., Steinmetz, N., Reddy, C. B., Carandini, M., and Harris, K. D. Spontaneous behaviors drive multidimensional, brainwide activity. *Science*, 364(6437):eaav7893, Apr. 2019. doi: 10.1126/science.aav7893.
32. Meshulam, L., Gauthier, J. L., Brody, C. D., Tank, D. W., and Bialek, W. Coarse graining, fixed points, and scaling in a large population of neurons. *Physical Review Letters*, 123:178103, 2019. doi: 10.1103/PhysRevLett.123.178103.
33. Stringer, C., Pachitariu, M., Steinmetz, N., Carandini, M., and Harris, K. D. High-dimensional geometry of population responses in visual cortex. *Nature*, 2019. doi: 10.1038/s41586-019-1346-5.
34. Morrell, M. C., Sederberg, A. J., and Nemenman, I. Latent dynamical variables produce signatures of spatiotemporal criticality in large biological systems. *Physical Review Letters*, 126:118302, 2021. doi: 10.1103/PhysRevLett.126.118302.

35. Hu, Y. and Sompolinsky, H. The spectrum of covariance matrices of randomly connected recurrent neuronal networks with linear dynamics. *PLoS Computational Biology*, 18, 7 2022. doi: 10.1371/journal.pcbi.1010327.
36. Morales, G. B., di Santo, S., and Muñoz, M. A. Quasiuniversal scaling in mouse-brain neuronal activity stems from edge-of-instability critical dynamics. *Proceedings of the National Academy of Sciences*, 120(9):e2208998120, Feb. 2023. doi: 10.1073/pnas.2208998120. Publisher: Proceedings of the National Academy of Sciences.
37. Cong, L., Wang, Z., Chai, Y., Hang, W., Shang, C., Yang, W., Bai, L., Du, J., Wang, K., and Wen, Q. Rapid whole brain imaging of neural activity in freely behaving larval zebrafish (Danio rerio). *eLife*, 6:e28158, Sept. 2017. doi: 10.7554/eLife.28158.
38. Chen, X., Mu, Y., Hu, Y., Kuan, A. T., Nikitchenko, M., Randlett, O., Chen, A. B., Gavornik, J. P., Sompolinsky, H., Engert, F., and Ahrens, M. B. Brain-wide Organization of Neuronal Activity and Convergent Sensorimotor Transformations in Larval Zebrafish. *Neuron*, 100(4):876–890.e5, Nov. 2018. doi: 10.1016/j.neuron.2018.09.042.
39. Mézard, M., Parisi, G., and Zee, A. Spectra of euclidean random matrices. *Nuclear Physics B*, 559(3):689–701, Oct. 1999. doi: 10.1016/S0550-3213(99)00428-9.
40. Cox, T. and Cox, M. *Multidimensional Scaling*. Chapman and Hall/CRC, 0 edition, Sept. 2000. ISBN 978-0-367-80170-0. doi: 10.1201/9780367801700. URL https://www.taylorfrancis.com/books/9781420036121.
41. Maaten, L. v. d. and Hinton, G. Visualizing Data using t-SNE. *Journal of Machine Learning Research*, 9(86):2579–2605, 2008.
42. Marques, J. C., Li, M., Schaak, D., Robson, D. N., and Li, J. M. Internal state dynamics shape brainwide activity and foraging behaviour. *Nature*, 577(7789):239–243, Jan. 2020. doi: 10.1038/s41586-019-1858-z.
43. Bianco, I. H., Kampff, A. R., and Engert, F. Prey Capture Behavior Evoked by Simple Visual Stimuli in Larval Zebrafish. *Frontiers in Systems Neuroscience*, 5, 2011. doi: 10.3389/fnsys.2011.00101.
44. Semmelhack, J. L., Donovan, J. C., Thiele, T. R., Kuehn, E., Laurell, E., and Baier, H. A dedicated visual pathway for prey detection in larval zebrafish. *eLife*, 3:e04878, Dec. 2014. doi: 10.7554/eLife.04878.
45. Dahmen, D., Grün, S., Diesmann, M., and Helias, M. Second type of criticality in the brain uncovers rich multiple-neuron dynamics. *Proceedings of the National Academy of Sciences*, 116(26):13051–13060, June 2019. doi: 10.1073/pnas.1818972116.
46. Kardar, M. *Statistical Physics of Fields*. Cambridge University Press, Cambridge, 2007. ISBN 978-0-521-87341-3. doi: 10.1017/CBO9780511815881. URL https://www.cambridge.org/core/books/statistical-physics-of-fields/06F49D11030FB3108683F413269DE945.
47. Beggs, J. M. and Plenz, D. Neuronal Avalanches in Neocortical Circuits. *Journal of Neuroscience*, 23(35):11167–11177, Dec. 2003. doi: 10.1523/JNEUROSCI.23-35-11167.2003.
48. Petermann, T., Thiagarajan, T. C., Lebedev, M. A., Nicolelis, M. A. L., Chialvo, D. R., and Plenz, D. Spontaneous cortical activity in awake monkeys composed of neuronal avalanches. *Proceedings of the National Academy of Sciences*, 106(37):15921–15926, Sept. 2009. doi: 10.1073/pnas.0904089106.
49. Bak, P., Tang, C., and Wiesenfeld, K. Self-organized criticality: An explanation of the 1/f noise. *Physical Review Letters*, 59(4):381–384, July 1987. doi: 10.1103/PhysRevLett.59.381.
50. Touboul, J. and Destexhe, A. Power-law statistics and universal scaling in the absence of criticality. *Physical Review E*, 95(1):012413, Jan. 2017. doi: 10.1103/PhysRevE.95.012413.
51. Kadanoff, L. P. Scaling laws for ising models near ${T}_{c}$. *Physics Physique Fizika*, 2(6):263–272, June 1966. doi: 10.1103/PhysicsPhysiqueFizika.2.263.
52. Bradde, S. and Bialek, W. PCA Meets RG. *Journal of Statistical Physics*, 167(3):462–475, May 2017. doi: 10.1007/s10955-017-1770-6.
53. Meshulam, L., Gauthier, J. L., Brody, C. D., Tank, D. W., and Bialek, W. Coarse–graining and hints of scaling in a population of 1000+ neurons, Dec. 2018. URL http://arxiv.org/abs/1812.11904. arXiv:1812.11904 [physics, q-bio].
54. Cohen, M. R. and Kohn, A. Measuring and interpreting neuronal correlations. *Nature Neuroscience*, 14(7):811–819, July 2011. doi: 10.1038/nn.2842.
55. Zhang, H., Rich, P. D., Lee, A. K., and Sharpee, T. O. Hippocampal spatial representations exhibit a hyperbolic geometry that expands with experience. *Nature Neuroscience*, 26(1):131–139, Jan. 2023. doi: 10.1038/s41593-022-01212-4.
56. Giusti, C., Pastalkova, E., Curto, C., and Itskov, V. Clique topology reveals intrinsic geometric structure in neural correlations. *Proceedings of the National Academy of Sciences*, 112(44):13455–13460, Nov. 2015. doi: 10.1073/pnas.1506407112.
57. Karoui, N. E. The spectrum of kernel random matrices. *The Annals of Statistics*, 38(1):1 – 50, 2010. doi: 10.1214/08-AOS648.
58. Muto, A., Lal, P., Ailani, D., Abe, G., Itoh, M., and Kawakami, K. Activation of the hypothalamic feeding centre upon visual prey detection. *Nature Communications*, 8(1):15029, Apr. 2017. doi: 10.1038/ncomms15029.
59. Bordenave, C. Eigenvalues of Euclidean random matrices. *Random Structures and Algorithms*, 33(4):515–532, Dec. 2008. doi: 10.1002/rsa.20228.
60. Rudin, W. *Fourier Analysis on Groups*. Wiley, 1 edition, Jan. 1990. ISBN 978-0-470-74481-9 978-1-118-16562-1. doi: 10.1002/9781118165621. URL https://onlinelibrary.wiley.com/doi/book/10.1002/9781118165621.
61. Leeuw, J. d. and Mair, P. Multidimensional Scaling Using Majorization: SMACOF in R. *Journal of Statistical Software*, 31:1–30, Aug. 2009. doi: 10.18637/jss.v031.i03.
62. Knapp, T. R. Canonical correlation analysis: a general parametric significance-testing system. *Psychological Bulletin*, 85(2):410, 1978.
63. Abbott, J. J., Peyer, K. E., Lagomarsino, M. C., Zhang, L., Dong, L., Kaliakatsos, I. K., and Nelson, B. J. How Should Microrobots Swim? *The International Journal of Robotics Research*, 28(11-12):1434–1447, Nov. 2009. doi: 10.1177/0278364909341658.
64. Mathis, A., Mamidanna, P., Cury, K. M., Abe, T., Murthy, V. N., Mathis, M. W., and Bethge, M. DeepLabCut: markerless pose estimation of user-defined body parts with deep learning. *Nature Neuroscience*, 21(9):1281–1289, Sept. 2018. doi: 10.1038/s41593-018-0209-y.
65. Tabor, K. M., Marquart, G. D., Hurt, C., Smith, T. S., Geoca, A. K., Bhandiwad, A. A., Subedi, A., Sinclair, J. L., Rose, H. M., Polys, N. F., and Burgess, H. A. Brain-wide cellular resolution imaging of Cre transgenic zebrafish lines for functional

circuit-mapping. *eLife*, 8:e42687, Feb. 2019. doi: 10.7554/eLife.42687.
66. Studholme, C., Hill, D. L. G., and Hawkes, D. J. Automated three-dimensional registration of magnetic resonance and positron emission tomography brain images by multiresolution optimization of voxel similarity measures. *Medical Physics*, 24(1):25–35, 1997. doi: 10.1118/1.598130.
67. Rueckert, D., Sonoda, L., Hayes, C., Hill, D., Leach, M., and Hawkes, D. Nonrigid registration using free-form deformations: application to breast MR images. *IEEE Transactions on Medical Imaging*, 18(8):712–721, Aug. 1999. doi: 10.1109/42.796284.
68. Rohlfing, T. Computational morphometry toolkit (cmtk), 2011. URL https://www.nitrc.org/projects/cmtk/.
69. Friedrich, J., Zhou, P., and Paninski, L. Fast online deconvolution of calcium imaging data. *PLOS Computational Biology*, 13 (3):e1005423, Mar. 2017. doi: 10.1371/journal.pcbi.1005423.
70. Umeyama, S. Least-squares estimation of transformation parameters between two point patterns. *IEEE Transactions on Pattern Analysis & Machine Intelligence*, 13(04):376–380, 1991.
71. Reynolds, D. Gaussian Mixture Models. In Li, S. Z. and Jain, A., editors, *Encyclopedia of Biometrics*, pages 659–663. Springer US, Boston, MA, 2009. ISBN 978-0-387-73003-5. doi: 10.1007/978-0-387-73003-5_196. URL https://doi.org/10.1007/978-0-387-73003-5_196.
72. Bezanson, J., Edelman, A., Karpinski, S., and Shah, V. B. Julia: A fresh approach to numerical computing. *SIAM review*, 59 (1):65–98, 2017.
73. Goetschy, A. and Skipetrov, S. Euclidean random matrices and their applications in physics. *arXiv preprint arXiv:1303.2880*, 2013. doi: 10.48550/ARXIV.1303.2880.

5 Supplementary Methods (S1)

5.1 Experimental methods

The handling and care of the zebrafish complied with the guidelines and regulations of the Animal Resources Center of the University of Science and Technology of China (USTC). All larval zebrafish (huc:h2b -GCaMP6f) were raised in E2 embryo medium (comprising 7.5 mM NaCl, 0.25 mM KCl, 0.5 mM $MgSO_4$, 0.075 mM KH_2PO_4, 0.025 mM Na_2HPO_4, 0.5 mM $CaCl_2$, and 0.35 mM $NaHCO_3$; containing 0.5 mg/L methylene blue) at 28.5 ℃ and with a 14-h light and 10-h dark cycle.

To induce hunting behavior in larval zebrafish, we fed them a large amount of paramecia over a period of 4-5 days post-fertilization (dpf). The animals were then subjected to a 24 hour starvation period, after which they were transferred to a specialized experimental chamber. The experimental chamber was 20mm in diameter and 1mm in depth, and the head of each zebrafish was immobilized by applying 2% low melting point agarose. The careful removal of the agarose from the eyes and tail of the fish ensured that these body regions remained free to move during hunting behavior. Thus, characteristic behavioral features such as J-turns and eye convergence could be observed and analyzed. Subsequently, the zebrafish were transferred to an incubator and stayed overnight. At 7 dpf, several paramecia were introduced in front of the previously immobilized animals, each of which was monitored by a stereomicroscope. Those displaying binocular convergence were selected for subsequent Ca^{2+} imaging experiments.

We developed a novel optomagnetic system (63) that allows (1) precise control of the trajectory of the paramecium and (2) imaging brain-wide Ca^{2+} activity during the hunting behavior of zebrafish. To control the movement of the paramecium, we treated these microorganisms with a suspension of ferric tetroxide for 30 minutes and selected those that responded to its magnetic attraction. A magnetic paramecium was then placed in front of a selected larva, and its movement was controlled by changing the magnetic field generated by Helmholtz coils that were integrated into the imaging system. The real-time position of the paramecium, captured by an infrared camera, was identified by online image processing. The positional vector relative to a predetermined target position was calculated. The magnitude and direction of the current in the Helmholtz coils were adjusted accordingly, allowing for precise control of the magnetic field and hence the movement of the paramecium. Multiple target positions could be set to drive the paramecium back and forth between multiple locations.

The experimental setup consisted of head-fixed larval zebrafish undergoing two different types of behavior: induced hunting behavior by a moving paramecium in front of a fish (fish 1-5), and spontaneous behavior without any visual stimulus (fish 6). Experiments were carried out at ambient temperature (ranging from 23℃ to 25℃). The behavior of the zebrafish was monitored by a high speed infrared camera (Basler acA2000-165umNIR, 0.66x) behind a 4F optical system and recorded at 50 Hz. Brain-wide Ca^{2+} imaging was achieved using XLFM. Light-field images were acquired at 10 Hz, using customized LabVIEW software (National Instruments, USA) or Solis software (Oxford Instruments, UK), with the help of a high-speed data acquisition card (PCIe-6321, National Instruments, USA) to synchronize the fluorescence with behavioral imaging.

5.1.1 Behavior analysis. The background of each behavior video was removed using the clone stamp tool in Adobe Photoshop CS6. Individual images were then processed by an adaptive thresholding algorithm, and fish head and yolk were selected manually to determine the head orientation. The entire body centerline, extending from head to tail, was divided into 20 segments. The amplitude of a bending segment was defined as the angle between the segment and the head orientation. To identify the paramecium in a noisy environment, we subtracted a background image, averaged over a time window of 100 s, from all the frames. The major axis of the left or right eye was identified using DeepLabCut (64). The eye orientation was defined as the angle between the rostrocaudal axis and the major axis of an eye; The convergence angle was defined as the angle between the major axes of the left and right eyes. An eye-convergence event was defined as a period of time where the angle between the long axis of the eyes stayed above 50 degrees (43).

5.1.2 Imaging data acquisition and processing. We used a fast eXtended light field microscope (XLFM, with a volume rate of 10 Hz) to record Ca^{2+} activity throughout the brain of head-fixed larval zebrafish. Fish were ordered by the dates of experiments. As previously described (37), we adopted the Richardson-Lucy deconvolution method to iteratively reconstruct 3D fluorescence stacks (600 × 600 × 250) from the acquired 2D images (2048 × 2048). This algorithm requires an experimentally measured point spread function (PSF) of the XLFM system.

To perform image registration and segmentation, we first cropped and resized the original image stack to 400 x 308 x 210, which corresponded to the size of a standard zebrafish brain (zbb) atlas (65). This step aimed to reduce substantial memory requirements and computational costs in subsequent operations. Next, we picked a typical volume frame and aligned it with the zbb atlas using a basic 3D affine transformation. This transformed frame was used as a template. We aligned each volume with the template using rigid 3D intensity-based registration (66) and non-rigid pairwise registration (67) in the Computational Morphometry Toolkit (CMTK) (68). After voxel registration, we computed the pairwise correlation between nearby voxel intensities and performed the watershed algorithm on the correlation map to cluster and segment voxels into consistent ROIs across all volumes. We defined the diameter of each ROI using the maximum Feret diameter (the longest distance between any two voxels within a single ROI).

Finally, we adopted the "OASIS" deconvolution method to denoise and infer neural activity from the fluorescence time sequence (69). The deconvolved $\Delta F/F$ of each ROI was used to infer firing rates for subsequent analysis.

5.2 Other experimental datasets analyzed

Dataset	Data Reference
Light-sheet imaging of larval zebrafish (38)	https://janelia.figshare.com/articles/dataset/Whole-brain_light-sheet_imaging_data/7272617
Neuropixels recordings in mice (31)	https://janelia.figshare.com/articles/dataset/Eight-probe_Neuropixels_recordings_during_spontaneous_behaviors/7739750
Two-photon imaging in mice (31)	https://janelia.figshare.com/articles/dataset/Recordings_of_ten_thousand_neurons_in_visual_cortex_during_spontaneous_behaviors/6163622

Table 2. Resources for additional experimental datasets

To validate our findings across different recording methods and animal models, we also analyzed three additional datasets. We include a brief description below for completeness. Further details can be found in the respective reference. The first dataset includes whole-brain light-sheet Ca^{2+} imaging of immobilized larval zebrafish in the presence of visual stimuli as well as in a spontaneous state (38). Each volume of the brain was scanned through 2.11$\pm$0.21 planes per sec, providing a near-simultaneous readout of neuronal Ca^{2+} signals. We analyzed fish 8 (69,207 neurons $\times$ 7,890 frames), 9 (79,704 neurons $\times$ 7,720 frames) and 11 (101,729 neurons $\times$ 8,528 frames), which are the first three fish data with more than 7,200 frames. For simplicity, we labeled them l2, l3, and l1(fl). The second dataset consists of Neuropixels recordings from approximately ten different brain areas in mice during spontaneous behavior (31). Data from the three mice, *Kerbs*, *Robbins*, and *Waksman*, include the firing rate matrices of 1,462 neurons $\times$ 39,053 frames, 2,296 neurons $\times$ 66,409 frames, and 2,688 neurons $\times$ 74,368 frames, respectively. The last dataset comprises two-photon Ca^{2+} imaging data (2-3 Hz) obtained from the visual cortex of mice during spontaneous behavior. While this dataset includes numerous animals, we focused on the first three animals that exhibited spontaneous behavior:`spont_M150824_MP019_2016-04-05`

(11,983 neurons $\times$ 21,055 frames), `spont_M160825_MP027_2016-12-12` (11,624 neurons $\times$ 23,259 frames), and `spont_M160907_MP028_2016-09-26` (9,392 neurons $\times$ 10,301 frames) (31).

5.3 Collapse index

In the definition of CI ,

$$\mathrm{CI} := \frac{1}{\log(q_0/q_1)} \int_{\log q_1}^{\log q_0} \left| \frac{\partial \log \lambda(q)}{\partial \log \rho} \right| \mathrm{d} \log q, \tag{18}$$

we set q_1 such that $\lambda(q_1) = 1$, which is the mean of the eigenvalues of a normalized covariance matrix . The other integration limit q_0 is set to 0.01 such that $\lambda(q_0)$ is the 1% largest eigenvalue.

5.3.1 A calculation of collapse index for experimental datasets/ERM model. To calculate CI for a covariance matrix C of size N_0, we first computed its eigenvalues λ_i^0 and those of the subsampled block C_s of size $N_s = N_0/2$, denoted as λ_i^s (averaged over 20 times for the ERM simulation in Fig. S4 and 2000 times in other figures). Next, we estimated $\log \lambda(q)$ using the eigenvalues of C_0 and C_s at $q = i/N_s$, $i = 1, 2, \ldots, N_s$. For the subsampled C_s, we simply had $\log \lambda(q = i/N_s) = \log \lambda_i^s$, its i-th largest eigenvalue. For the original C_0, $\log \lambda(q = i/N_s)$ was estimated by a linear interpolation, *on the* $\log \lambda$-$\log q$ *scale*, using the value of $\log \lambda(q)$ in the nearest neighboring $q = i/N_0$'s (which again are simply $\log \lambda_i^0$). Finally, the integral (Eq. (18)) was computed using the trapezoidal rule, discretized at $q = i/N_s$' s, using the finite difference $\frac{\partial \log \lambda(q)}{\partial \log \rho} \approx \frac{1}{\log(N_0/N_s)} |\Delta \log \lambda(q)|$, where Δ denotes the difference between the original eigenvalues of C_0 and those of subsampled C_s.

5.3.2 Estimating CI using the variational method. In the definition of CI (Eq. (18)) , calculating $\lambda(q)$ and $\frac{\partial \log \lambda(q)}{\partial \log \rho}$ directly using the variational method is difficult, but we can make use of an implicit differentiation

$$\frac{\partial \log \lambda(q, \rho)}{\partial \log \rho} = \frac{\rho}{\lambda} \frac{\partial \lambda(q, \rho)}{\partial \rho} = -\frac{\rho}{\lambda} \frac{\frac{\partial q(\rho, \lambda)}{\partial \rho}}{\frac{\partial q(\rho, \lambda)}{\partial \lambda}}, \tag{19}$$

where $q(\lambda) := \int_\lambda^\infty p(\lambda) \mathrm{d}\lambda$ is the complementary cdf (the inverse function of $\lambda(q)$ in section 5.3.1). Using this, the integral in CI (Eq. (18)) can be rewritten as

$$\int_{\log q_1}^{\log q_0} \left| \frac{\partial \log \lambda(q, \rho)}{\partial \log \rho} \right| \mathrm{d} \log q = \int_{q_1}^{q_0} \left| -\frac{\rho}{q\lambda} \frac{\frac{\partial q}{\partial \rho}}{\frac{\partial q}{\partial \lambda}} \right| \mathrm{d}q = \int_{\lambda(q_1)}^{\lambda(q_0)} \left| -\frac{\rho}{q\lambda} \frac{\frac{\partial q}{\partial \rho}}{\frac{\partial q}{\partial \lambda}} \right| \frac{\partial q}{\partial \lambda} \mathrm{d}\lambda = \int_{\lambda(q_0)}^{\lambda(q_1)} \left| \frac{1}{\lambda} \frac{\partial \log q}{\partial \log \rho} \right| \mathrm{d}\lambda. \tag{20}$$

Since $\frac{\partial q}{\partial \lambda} = -p(\lambda) < 0$, we switch the order of the integration interval in the final expression of Eq. (20).

First, we explain how to compute the complementary cdf $q(\lambda)$ numerically using the variational method. The key is to integrate the probability density function $p(\lambda)$ from λ to a finite $\lambda(q_s)$ rather than to infinity,

$$q(\lambda) = \int_\lambda^\infty p(\lambda) \mathrm{d}\lambda = \int_{\lambda(q_s)}^\infty p(\lambda) \mathrm{d}\lambda + \int_\lambda^{\lambda(q_s)} p(\lambda) \mathrm{d}\lambda = q_s + \int_\lambda^{\lambda(q_s)} p(\lambda) \mathrm{d}\lambda. \tag{21}$$

The integration limit $\lambda(q_s)$ cannot be calculated directly using the variational method. We thus used the value of $\lambda^s(q_s \approx q_0)$ (section 5.3) from *simulations of the ERM with a large* $N = 1024$ as an approximation. Furthermore, we employed a smoothing technique to reduce bias in the estimation of $\lambda^s(q_s)$ due to the leading zigzag eigenvalues (i.e., the largest eigenvalues) of the eigenspectrum. Specifically, we determined the nearest rank $j < Nq_0$ and then smoothed the eigenvalue $\log \lambda^s(q_s)$ on the log-log scale using the formula $\log \lambda^s(q_s) = \frac{1}{3} \sum_{i=0}^{2} \log \lambda^s(\frac{j+i}{N})$ and $\log q_s = \frac{1}{3} \sum_{i=0}^{2} \log \frac{j+i}{N}$, averaging over 100 ERM simulations.

Note that we can alternatively use the *high density theory* (S3) to compute the integration limit $\lambda(q_s = 1/N)$ instead of resorting to simulations. However, since the true value deviates from the $\lambda^h(q_s = 1/N)$ derived from high density theory, this approach introduces a constant bias (Fig. S6) when computing the integral in Eq. (21). Therefore we used the simulation value $\lambda^s(q_s \approx q_0)$ when producing Fig. 4B.

Next, we describe how each term within the integral of Eq. (20) was numerically estimated. First, we calculated $\frac{\partial \log q}{\partial \log \rho}$ with a similar method described in section 5.3.1. Briefly, we calculated $q_0(\lambda)$ for density $\rho_0 = \frac{N_0}{L^d}$ and $q_s(\lambda)$

for density $\rho_s = \frac{N_s}{L^d}$, and then used the finite difference $\frac{1}{\log(\rho_0/\rho_s)}|\Delta \log q(\lambda)|$. Second, $\frac{\partial \log q(\lambda)}{\partial \log \rho}$ was evaluated at $\lambda = \lambda(q_1) + i\frac{\lambda(q_0)-\lambda(q_1)}{k-1}$, where $i = 0, 1, 2, \ldots, k-1$, and we used $k = 20$. Finally, we performed a cubic spline interpolation of the term $\frac{\partial \log q}{\partial \log \rho}$, and obtained the theoretical CI by an integration of Eq. (20). Fig. S6A,B shows a comparison between theoretical CI and that obtained by numerical simulations of ERM (section 5.3.1).

5.4 Extensions of ERM and factors not affecting the scale invariance

In Results section 2.5 we considered five additional types of spatial density distributions (coordinate distributions) in functional space and two additional functional space geometries. We examined the points distributed according to the uniform distribution ($\vec{x} \sim 1/L^d$), the normal distribution ($\vec{x} \sim \mathcal{N}(\mu_p, \sigma_p^2\mathbf{I})$), and the log-normal distribution ($\log \vec{x} \sim \mathcal{N}(\mu_p, \sigma_p^2\mathbf{I})$). We used the method described in Methods section 4.3.1 to adjust the parameters of the coordinate distributions based on the uniform distribution case, so that they all generate similar pairwise correlation distributions. The relationships between these parameters are described in Methods section 4.3.1. In Fig. 5B, we used the following parameters: $d = 2$; $L = 10$ for the uniform distribution; $\mu_p = 0$, $\sigma_p = 2.82$ for the normal distribution; and $\mu_p = 2$, $\sigma_p = 0.39$ for the log-normal distribution.

Second, we introduced multiple clusters of neurons in the functional space, with each cluster uniformly distributed in a box. We considered three arrangements: (1) two closely situated clusters (with a box size of $L = 5\sqrt{2}$, the distance between two cluster centers being $L_c = L$), (2) two distantly situated clusters (with a box size of $L = 5\sqrt{2}$ and the distance between clusters $L_c = 4L$), and three clusters arranged symmetrically in an equilateral triangle (with a box size of $L = 10/\sqrt{3}$ and the distance between clusters $L_c = L$).

Finally, we examined the scenario in which the points were uniformly distributed on the surface of a sphere ($4\pi l^2 = L^2$, l being the radius of the sphere) or a hemisphere ($2\pi l^2 = L^2$) embedded in $\mathbb{R}^3$ (the pairwise distance is that in $\mathbb{R}^3$). It should be noted that both cases have the same surface area as the 2D box (Results section 2.5).

5.5 Analyzing the effects of removing neural activity data during hunting

To identify and remove the time frames corresponding to putative hunting behaviors, the following procedure was used. The hunting interval was defined as 10 frames (1 sec) preceding the onset of an eye convergence (section 5.1.1) to 10 frames after the offset of this eye convergence. These frames were then excluded from the data before recalculating the covariance matrix (see Methods section 4.1) and subsequently the subsampled eigenspectra (Fig. 7B, Fig. S14B,D,F,H). As a control to the removal of the hunting frame, an equal number of time frames that are not within those hunting intervals were randomly selected and then removed and analyzed (Fig. 7C, Fig. S14A,C,E,G). The number of hunting interval frames and total recording frames for five fish exhibiting hunting behaviors are as follows: fish 1 - 268/7495, fish 2 - 565/9774, fish 3 - 2734/13904, fish 4 - 843/7318 and fish 5 - 1066/7200. Fish 6 (number of time frames: 9388) was not exposed to a prey stimulus and, therefore, was excluded from the analysis.

To assess the impact of hunting removal on CI, we calculated the CI of the covariance matrix using all neurons recorded in each fish (without subsampling to 1024 neurons). For the control case, we repeated the removal of the nonhunting frame 10 times to generate 10 covariance matrices and computed their CIs. We used a one-sample t-test to determine the level of statistical significance between the control CIs and the CI obtained after removal of the hunting frame.

Using fitted ERM parameters by full data, we performed a MDS on the control data and hunting-removed data to infer the functional coordinates. Note that the functional coordinates inferred by MDS are not unique: rotations and translations give equivalent solutions. For visualization purposes (not needed for analysis), we first used the Umeyama algorithm (70) to optimally align the functional coordinates of control and hunting-removed data.

To identify distinct clusters within the functional coordinates, we fit Gaussian Mixture Models (GMMs, (71)) using the "GaussianMixtures" package in Julia (72). We chose the number of clusters K based on giving the smallest Bayesian Information Criterion (BIC) score. After fitting the GMMs, a list of probabilities p_{ik}, $k = 1, 2, \ldots, K$ was given for each neuron i specifying the probability of the neuron belonging to the cluster k. The mean and covariance parameters were estimated for each Gaussian distributed cluster. For visualization (but not for analysis), a neuron was colored according to cluster k^* where $k^* = \arg\max_{1 \le k \le K} p_{ik}$.

We used the following method to measure the size of the cluster and its fold change. For a 2D (recall $d = 2$ in our ERM) Gaussian distributed cluster, let us consider an ellipse centered on its mean, and its axes are aligned

with the eigenvectors of its covariance matrix $C_{2\times 2}$. Let the eigenvalues of C be λ_1, λ_2. Then we set the length of the half-axis of the ellipse to be $c\sqrt{\lambda_i}$, respectively. Here $c > 0$ is a constant determined below. Note that the ellipse axes correspond to linear combinations of 2D Gaussian random variables that are independent and λ_i's are the variance of these linear combinations. From this fact, it is straightforward to show that the probability that a sample from the Gaussian cluster lies in the above ellipse depends only on c, that is, $1 - e^{-\frac{c^2}{2}}$, and not on the shape of the cluster. So, the ellipse represents a region that covers a fixed proportion of neurons for any cluster, and its area can be used as a measure for the size of the Gaussian cluster. Note that the area of the ellipse is $\pi c^2 \sqrt{\lambda_1 \lambda_2} = \pi c^2 \sqrt{\det(C)}$. In Fig. S15, we plot the ellipses to help visualize the clusters and their changes. We choose c such that the ellipse covers 95% of the probability (that is, the fraction of neurons belonging to the cluster).

In the control functional map where we fit the GMMs, we directly calculated the size measure $\pi c^2 \sqrt{\det(C)}$ from the estimated covariance C for each Gaussian cluster. In the hunting-removed functional map, we needed to estimate the covariance C' for neurons belonging to a cluster k under the new coordinates (we assume that the new distribution can still be approximated by a Gaussian distribution). We performed this estimation in a probabilistic manner to avoid issues of highly overlapping clusters where the cluster membership could be ambiguous for some neurons. First, we estimated the center/mean of the new Gaussian distribution by

$$(\bar{x}, \bar{y}) := \left(\frac{\sum_{i=1}^{N} p_{ik} x_i}{\sum_{i=1}^{N} p_{ik}}, \frac{\sum_{i=1}^{N} p_{ik} y_i}{\sum_{i=1}^{N} p_{ik}} \right).$$

Here the summation goes over all the N neurons in the functional space and p_{ik} is the membership probability defined above, and (x_i, y_i) is the coordinate of neuron i in the hunting-removed map. Similarly, we can use a weighted average to estimate the entries in the covariance matrix $C' = \begin{bmatrix} C'_{xx} & C'_{xy} \\ C'_{yx} & C'_{yy} \end{bmatrix}$. For example,

$$\hat{C}'_{xy} := \frac{\sum_{i=1}^{N} p_{ik} (x_i - \bar{x})(y_i - \bar{y})}{\sum_{i=1}^{N} p_{ik}}.$$

Then we calculated the size of the cluster on the new map as $\pi c^2 \sqrt{\det(\hat{C}')}$. Finally, we computed the fold change in size as $\sqrt{\frac{\det(\hat{C}')}{\det(C)}}$.

5.6 Renormalization-Group (RG) Approach

Here we briefly summarize the RG approach (32) and elucidate the adjustments required when directly applying the RG approach to ERM. During each iterative procedure denoted k, Pearson's correlation coefficients for each pair of neurons were calculated. This yields the maximum correlated pair, designated as a and b. These pairs are unified according to the following equation:

$$x_i^k = Z_{ab}^{k-1} (x_a^{k-1} + x_b^{k-1}) \tag{22}$$

Z_{ab}^{k-1} is used to normalize the average to ensure that the nonzero activity of the new variables x_i^k is equal to one.

When the RG approach is applied directly to the ERM, the process differs slightly. Instead of combining neural activity, we merge correlation matrices to traverse different scales. During the kth iteration, we compute the coarse-grained covariance as

$$c_{ij}^k = c_{ab}^{k-1} + c_{ac}^{k-1} + c_{bc}^{k-1} + c_{bd}^{k-1} \tag{23}$$

and the variance as

$$c_{ii}^k = c_{aa}^{k-1} + c_{bb}^{k-1} + 2c_{ab}^{k-1} \tag{24}$$

Following these calculations, we normalize the coarse-grained covariance matrix to ensure that all variances are equal to one.

Finally, we calculate the eigenspectra of the covariance matrices across different cluster sizes, following the approach described in (32).

Consider a hypothetical scenario where a set of eight neurons, labeled $1, 2, 3, ..., 7, 8$, are subjected to a two-step clustering procedure. In the first step, neurons are grouped based on their maximum correlation pairs, resulting in the formation of four pairs: $\{1, 2\}, \{3, 4\}, \{5, 6\}$, and $\{7, 8\}$.

Subsequently, the neurons are further grouped into two clusters based on the results of the RG step mentioned above. Specifically, if the correlation between the coarse-grained variables of the pair $\{1, 2\}$ and the pair $\{3, 4\}$ is found to be the largest among all other pairs of coarse-grained variables, the first group consists of neurons $\{1, 2, 3, 4\}$, while the second group contains neurons $\{5, 6, 7, 8\}$.

Next, take the size of the cluster $N = 4$ for example. The eigenspectra of the covariance matrices of the four neurons within each cluster are computed. This results in two eigenspectra, one for each cluster. The correlation matrices used to compute the eigenspectra of different sizes do not involve coarse-grained neurons. It is the real neurons $1, 2, 3, ..., 7, 8$, but with expanding cluster sizes.

Finally, the average of the eigenspectra of the two clusters is calculated.

6 Supplementary figures (S2)

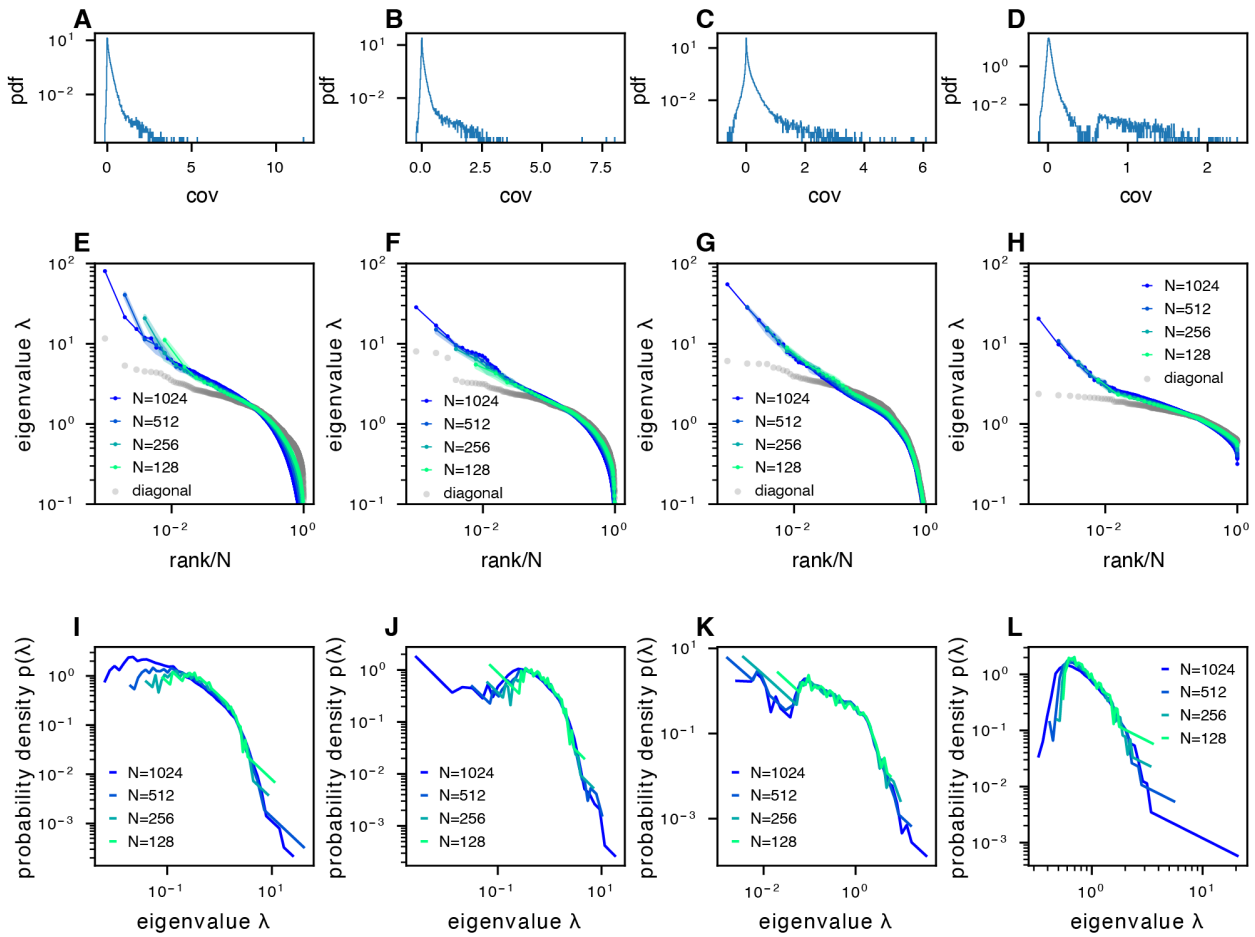

Figure S1. The phenomenon of scale-invariant eigenspectra across different datasets. A-D. Distribution of normalized pairwise covariances, where $\mathrm{E}(\sigma_i^2) = 1$ (Methods). **E-H.** Subsampled covariance eigenspectra of different datasets. **I-L.** Pdfs of subsampled covariance matrix eigenspectra of different datasets. The datasets correspond to the following examples: column 1: fish data (from fish 1, all fish data are shown in Fig. S9A-D) from whole brain light-field imaging; column 2: fish data from whole brain light-sheet imaging; column 3: mouse data from multi-area Neuropixels recording; column 4: mouse data from two-photon visual cortex recording.

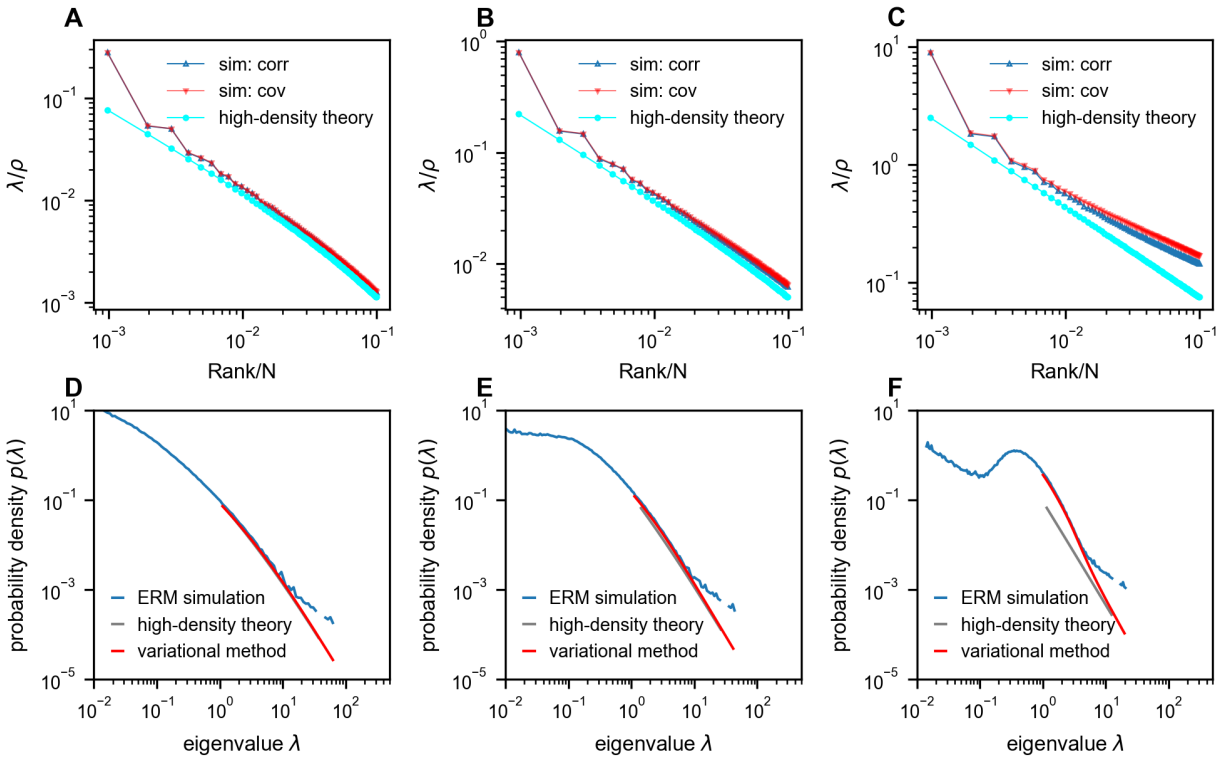

Figure S2. Comparison between ERM simulation and theory. A-C. Rank plots of the normalized eigenspectra (λ/ρ), with the simulations obtained using correlation matrix (sim: corr, $\sigma_i^2 = 1$) and covariance matrix (sim: cov, neuron's activity variance σ_i^2 is i.i.d. sampled from a log-normal distribution with zero mean and a standard deviation of 0.5 in the natural logarithm of the σ_i^2 values; we also normalize $\mathrm{E}(\sigma_i^2) = 1$ (Methods)). The curves between "sim: corr" and "sim: cov" are nearly identical in panels A and B. The theoretical predictions of normalized eigenvalues λ/ρ are obtained using the high-density theory (cyan, Eq. (10)). The density ρ decreases from panel A to panel C ($\rho = 1024, 256, 10.24$ respectively). **D-F.** Numerical validation of the theoretical spectrum by comparing probability density functions for increasing density of covariance ERM ($\rho = 1024, 256, 10.24$ respectively). Other simulation parameters: $N = 1024$, $d = 2$, $L = (N/\rho)^{1/d}$, $\mu = 0.5$, $\epsilon = 0.03125$. The ERM simulations were conducted 100 times. The results are presented as the mean ± SEM.

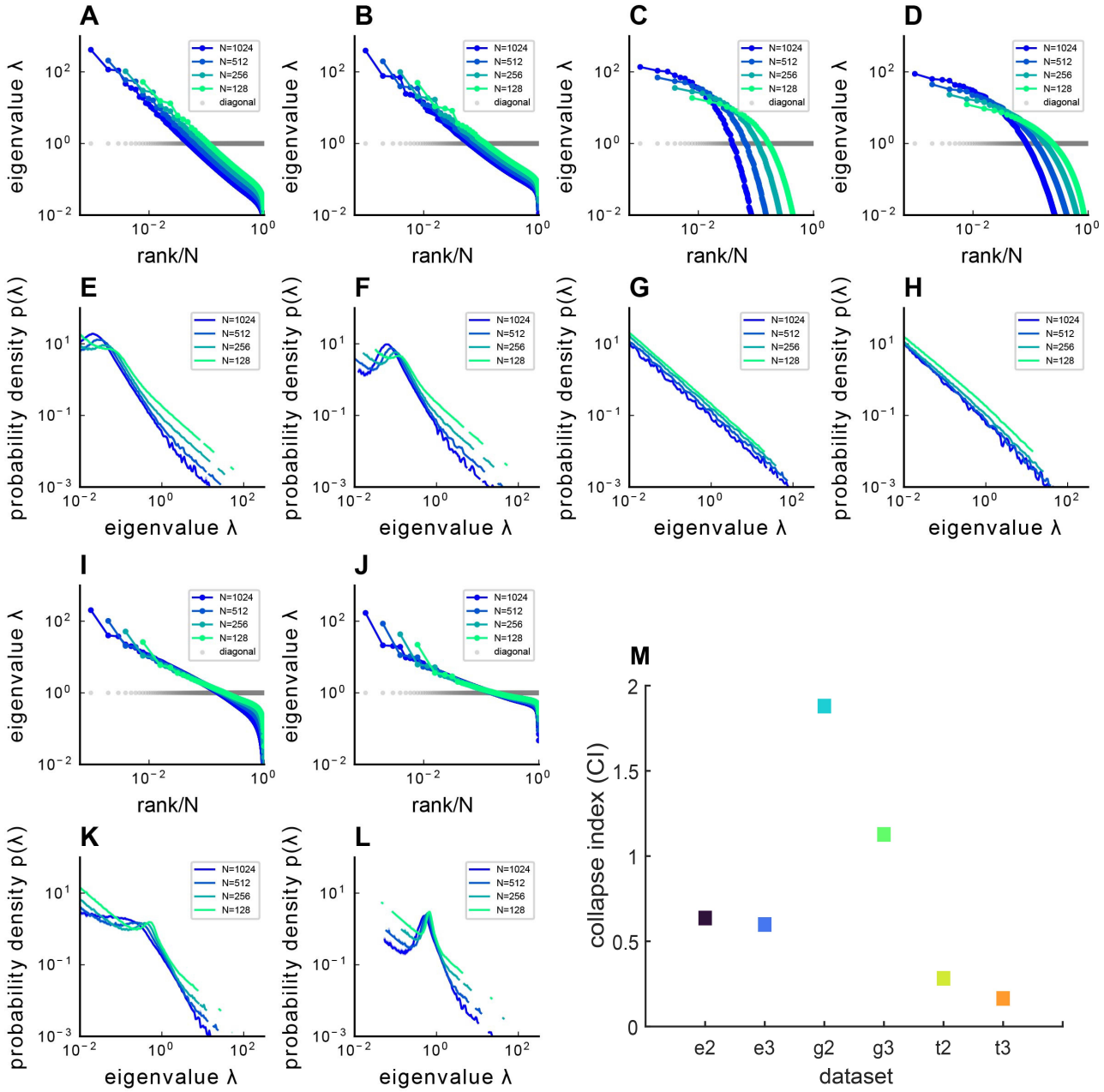

Figure S3. Covariance spectra under different kernel functions $f(\vec{x})$. The figure presents both the subsampled eigenvalue rank plot and the pdf of ERM with different functions $f(\vec{x})$ and varying dimensions d, where panels **A-D,I,J.** display the rank plot and panels **E-H,K,L.** show the pdf of ERM. **A,E.** Exponential function $f(\vec{x}) = e^{-\frac{\|x\|}{b}}$ and dimension $d = 2$. **B,F.** Exponential function $f(\vec{x}) = e^{-\frac{\|x\|}{b}}$ where $b = 1$ and dimension $d = 3$. **C,G.** Gaussian pdf $f(\vec{x}) = e^{-\frac{\|x\|^2}{2\sigma_x^2}}$ where $\sigma_x^2 = 0.1$ and dimension $d = 2$. **D,H.** Gaussian pdf $f(\vec{x}) = e^{-\frac{\|x\|^2}{2\sigma_x^2}}$ where $\sigma_x^2 = 0.1$ and dimension $d = 3$. **I,K.** t pdf (Eq. (2)) and dimension $d = 2$. **J,L.** t pdf (Eq. (2)) and dimension $d = 3$. The ERM simulations were conducted 100 times and each ERM used an identical subsampling technique described in (Methods). The results represent mean ± SEM. **M.** Summary of CI's for different $f(\vec{x})$ and d.

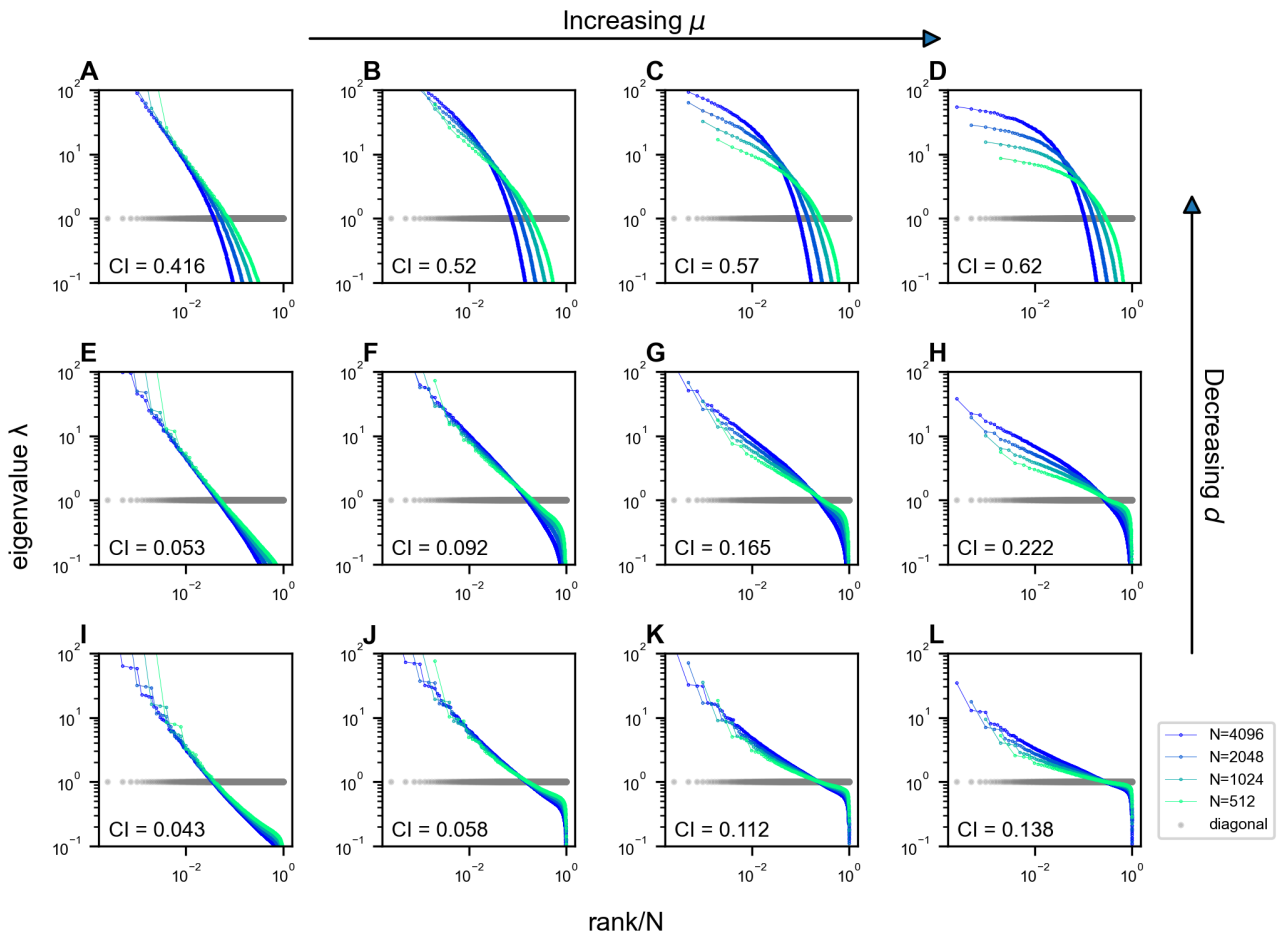

Figure S4. Impact of μ and d on the scale invariance of covariance eigenspectra in the ERM with t pdf $f(\vec{x})$ (Eq. (2)). The columns from left to right correspond to $\mu = 0.1, 0.5, 0.9, 1.3$, and the rows from top to bottom correspond to $d = 1, 2, 3$ (Eq. (1) and Eq. (2)). Other ERM simulation parameters: $N = 4096$, $\rho = 256$, $L = (N/\rho)^{1/d}$, $\epsilon = 0.03125$ and $\sigma_i^2 = 1$. Each panel is similar to Fig. 2D, but shows a single ERM realization. For visualization purposes, the views in some panels are truncated since we use the same range for the eigenvalues in all panels.

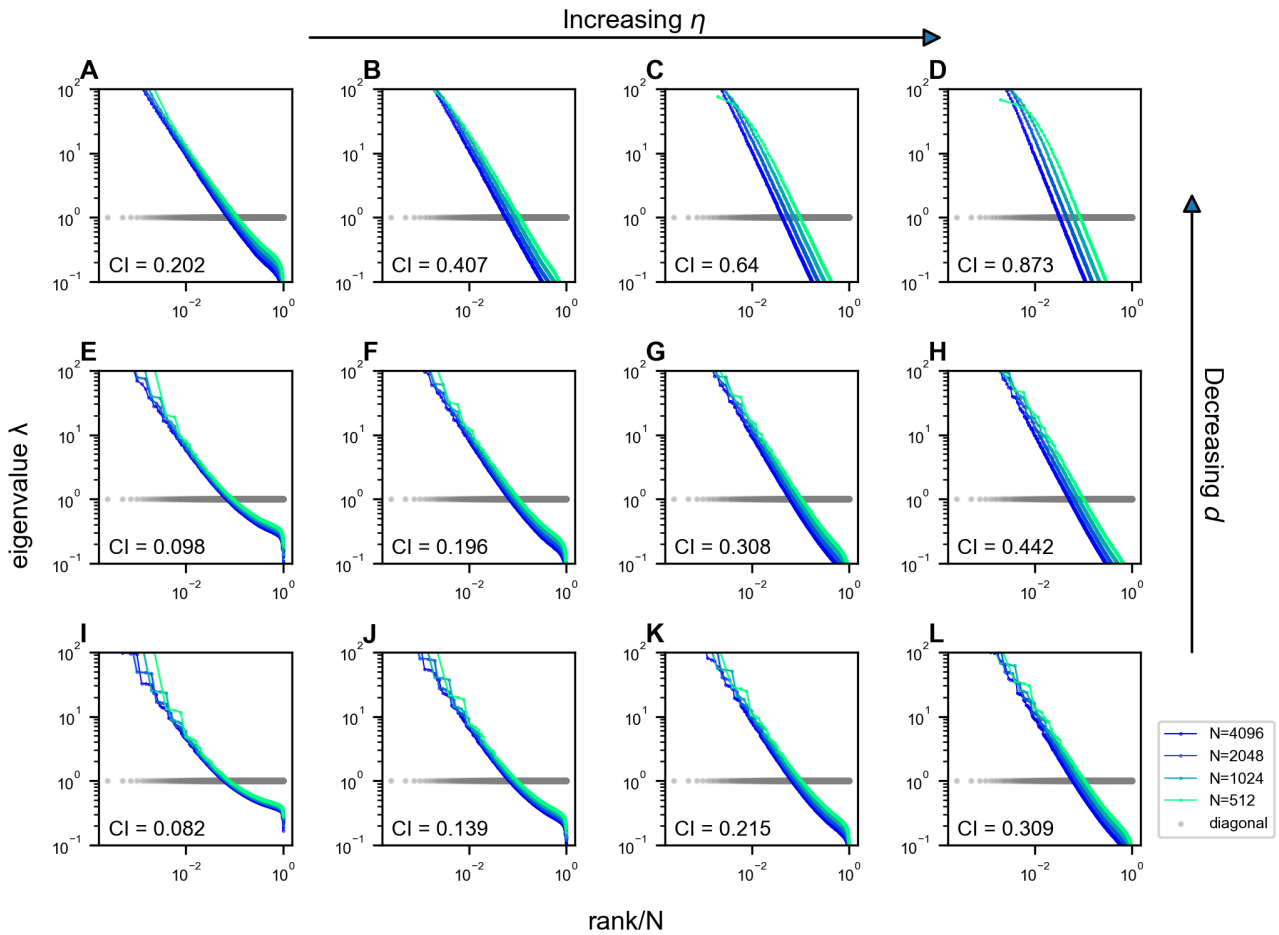

Figure S5. Impact of η and d on the scale invariance of covariance eigenspectra in the ERM with $f(\vec{x}) = e^{-\|\vec{x}\|^{\eta}}$. The columns from left to right correspond to $\eta = 0.3, 0.5, 0.7, 0.9$, and the rows from top to bottom correspond to $d = 1, 2, 3$ (Eq. (1) and Eq. (2)). Other ERM simulation parameters: $N = 4096$, $\rho = 256$, $L = (N/\rho)^{1/d}$, $\epsilon = 0.03125$ and $\sigma_i^2 = 1$. Each panel shows a single ERM realization. For visualization purposes, the views in some panels are truncated since we use the same range for the eigenvalues in all panels.

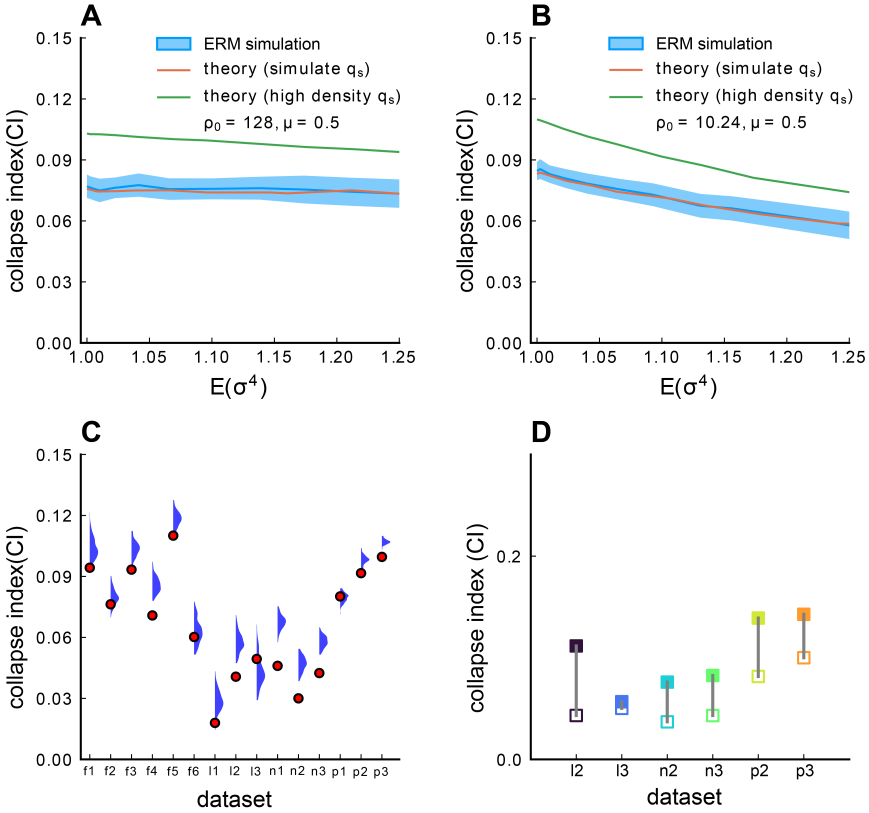

Figure S6. Impact of heterogeneous activity levels on the scale invariance. A. The CI as a function of the heterogeneity of neural activity levels $\mathrm{E}(\sigma_i^4)$. We generate ERM where each neuron's activity variance σ_i^2 is i.i.d. sampled from a log-normal distribution, with the same parameters as in Fig. 4B. The solid blue line is the average across 100 ERM simulations, and the shaded area represents the SD. The red line results from the Gaussian variational method with simulation value integration limit q_s^s (same as in Fig. 4B). The green line is the result of the Gaussian variational method with high-density value integration limit q_s^h (S1). $\rho_0 = 128$. **B.** Same as A, but with a smaller $\rho_0 = 10.24$. Other parameters: $\mu = 0.5$, $d = 2$, $N = 1024$, $L = (N/\rho)^{1/d}$, $\epsilon = 0.03125$. **C.** Comparison of the collapse index between the experimental data and shuffled data. Red dots represent the collapse index of experimental data, and blue shapes: are the collapse index distribution of shuffled data. Datasets: f1 to f6: six light-field zebrafish data (10 Hz per volume, S1); l1 (fl) to l3: light-sheet zebrafish data (2 Hz per volume); n1 (mn) to n3: Neuropixels mouse data, 30 Hz downsample to 10 Hz per volume, p1 (mp) to p3: two-photon mouse data, (3 Hz per volume). **D.** The collapse index (CI) of the correlation matrix (filled symbols) is larger than that of the covariance matrix (opened symbols) across different datasets excluding those shown in Fig. 4. We use 7,200 time frames data across all the datasets.

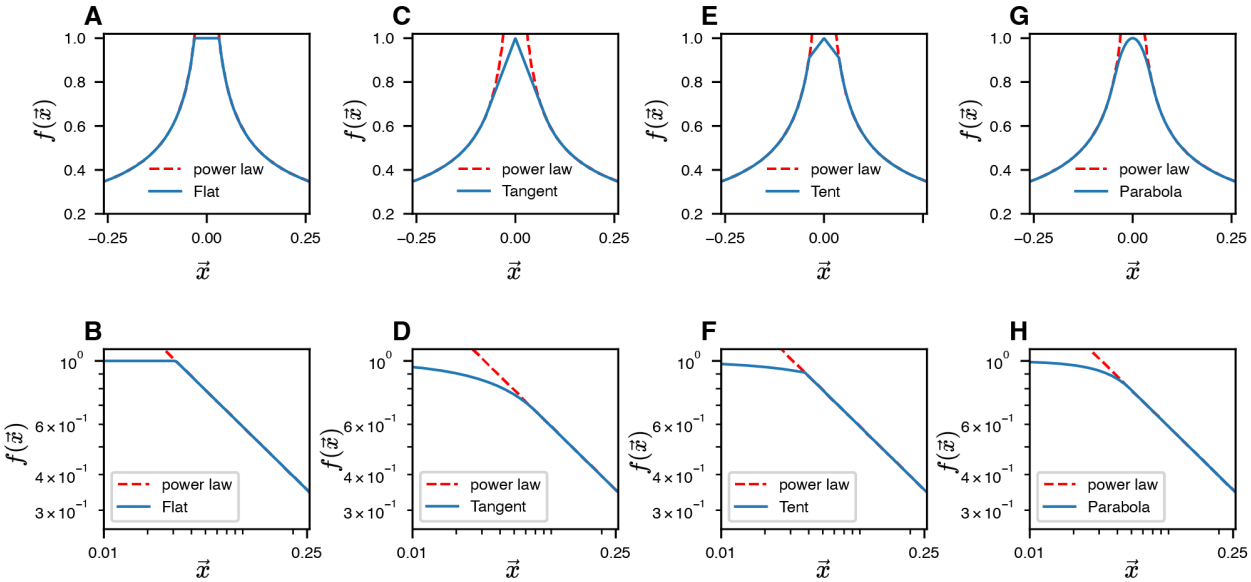

Figure S7. Modifications $f(\vec{x})$ near $x = 0$ other than the t pdf (table S3). The upper row illustrates the slow-decaying kernel function $f(\vec{x})$ (blue solid line) and its power-law asymptote (red dashed line) along a 1D slice at various $f(\vec{x})$. The lower row is similar to **A**, but on the log-log scale. The formulas for different $f(\vec{x})$'s are listed in table S3 in S3.

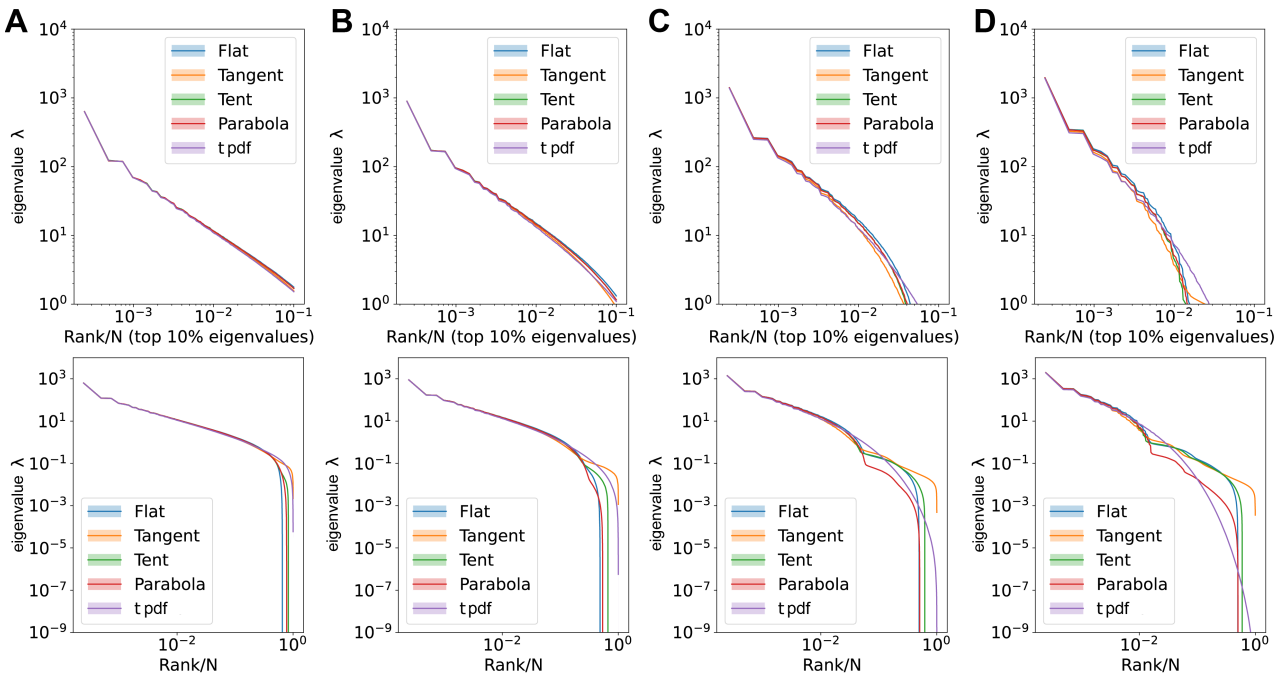

Figure S8. Comparisons of large eigenvalues across different smoothing interval sizes, ϵ. Rank plot (upper row) and pdf (lower row) of the covariance eigenspectrum for ERMs with different $f(\vec{x})$. **A.** $\epsilon = 0.06$. **B.** $\epsilon = 0.12$. **C.** $\epsilon = 0.3$. **D.** $\epsilon = 0.6$. Other ERM simulation parameters: $N = 4096$, $\rho = 100$, $\mu = 0.5$, $d = 2$, $L = 6.4$, $\sigma_i^2 = 1$. The formulas for different $f(\vec{x})$'s are listed in table S3 in S3.

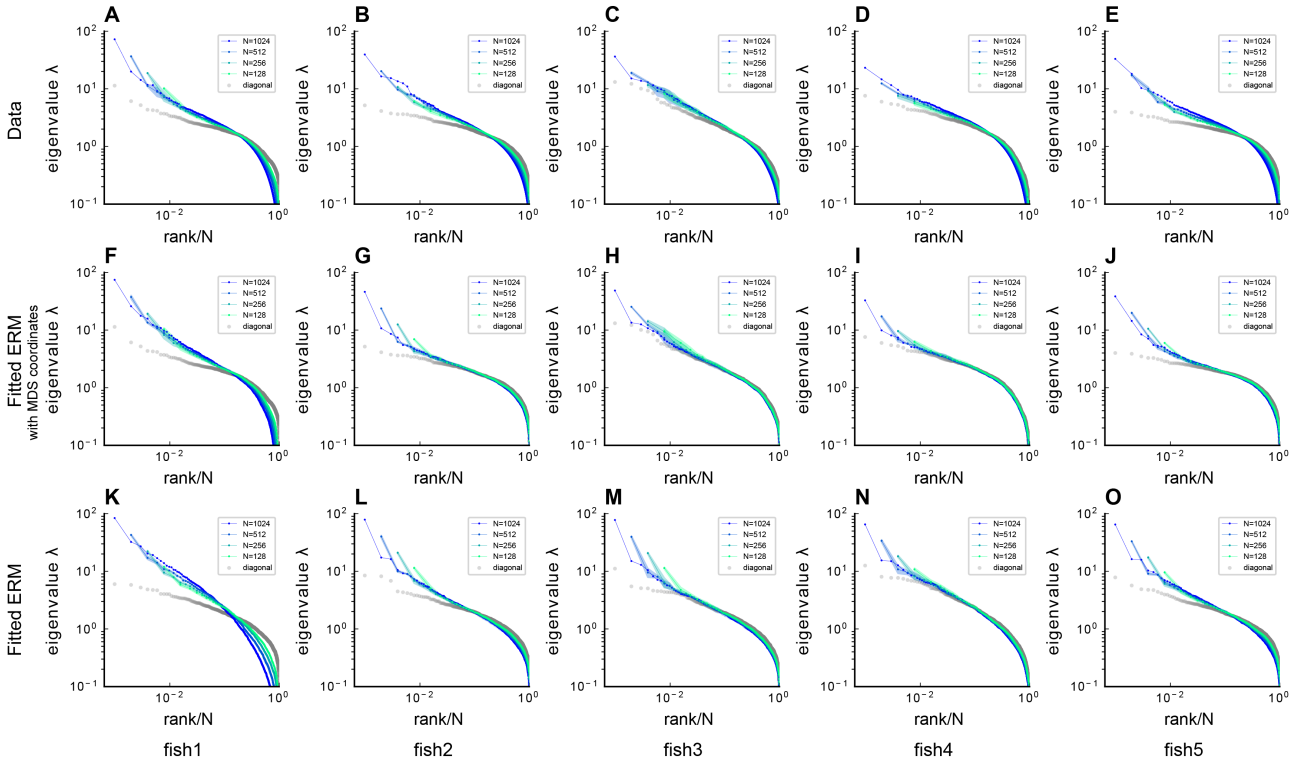

Figure S9. Fitting ERM to zebrafish data from our experiments (part 1). Comparison of subsampled covariance eigenspectra in fish data and fitted ERM models. The columns correspond to five light-field zebrafish data: fish 1 to fish 5 (results for fish 6 has been shown in Fig. 6). Number of time frames: fish 1 - 7495, fish 2 - 9774, fish 3 - 13904, fish 4 - 7318, and fish 5 - 7200. **A-E.** Subsampled covariance eigenspectra for different fish data. **F-J.** Same as A-E but for ERM models with fitted parameters (μ, L) and functional coordinates inferred using MDS and the experimental σ_i. **K-O.** Same as A-E but for ERM models with parameters (μ, L, distribution parameters of σ^2) fitted from different fish data.

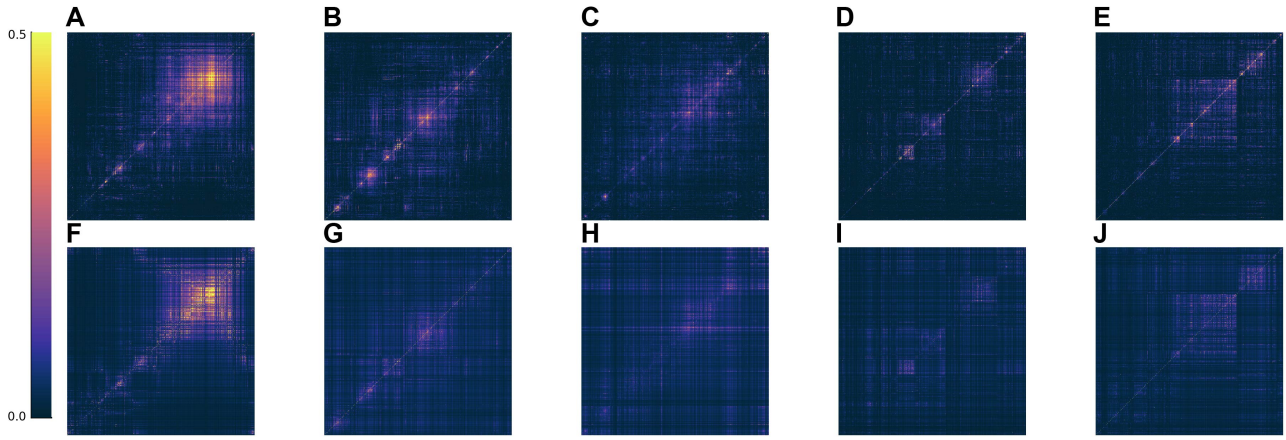

Figure S10. Fitting ERM to all six zebrafish data from our experiments (part 2). Comparison of the covariance matrix between fish data and our fitted model. The columns correspond to five light-field zebrafish data: fish 1 to fish 5 (with fish 6 has been shown in Fig. 6). **A-E.** The covariance matrix of different fish data. **F-J.** The covariance matrix of ERM models with fitted parameters (μ, L) and functional coordinates inferred using MDS and the experimental σ_i.

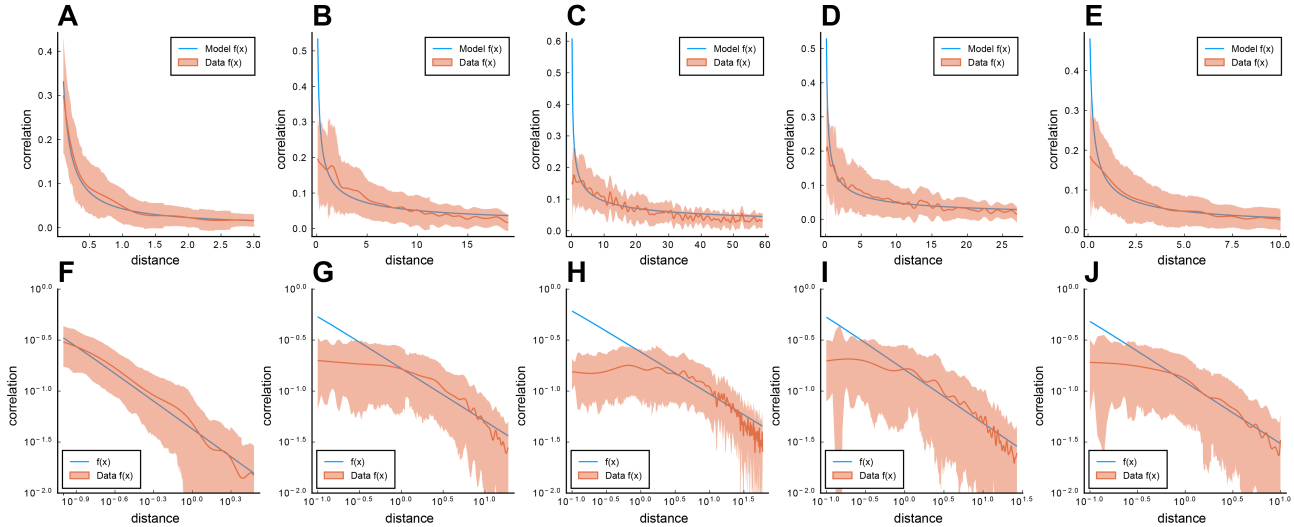

Figure S11. Fitting ERM to all six zebrafish data from our experiments (part 3). Similar to Fig. S10, columns correspond to five light-field zebrafish data: fish 1 to fish 5 (with fish 6 has been shown in Fig. 6). **A-E**: Comparison of the power-law kernel function $f(\vec{x})$ in the model (blue line) and the correlation-distance relationship in the data (red line). The distance is calculated from the inferred coordinates using MDS. The shaded area represents the SD. **F-J**: Same as A-D but on the log-log scale.

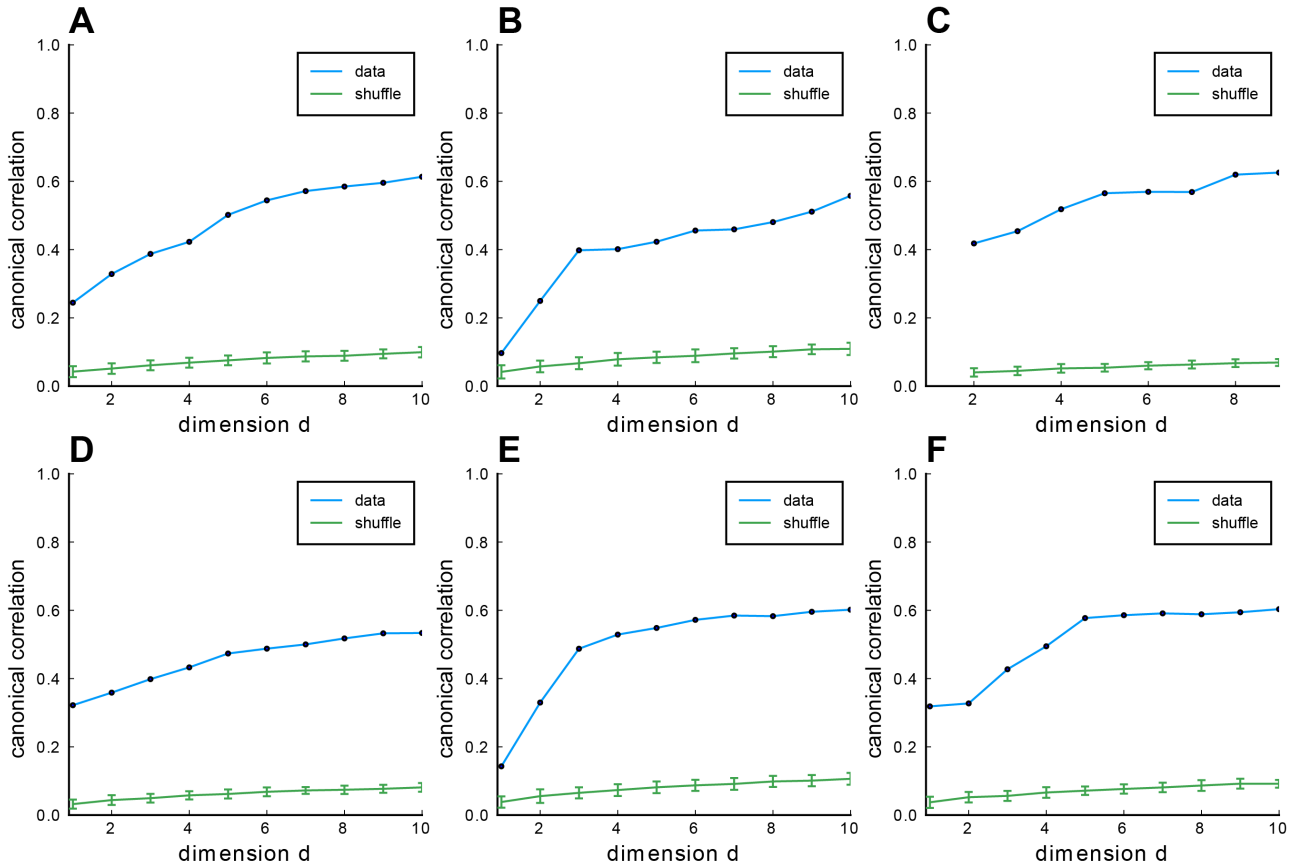

Figure S12. Fitting ERM to all six zebrafish data from our experiments (part 3). Similar to Fig. S10, columns correspond to 6 light-field zebrafish data: fish 1 to fish 6. **A-F**: CCA correlation between the first CCA variables with different embedding dimensions in the functional space. Blue line indicates the CCA correlation of example fish data, green line shows the CCA correlation of example fish data with shuffled functional coordinates, and error bars represent the SD.

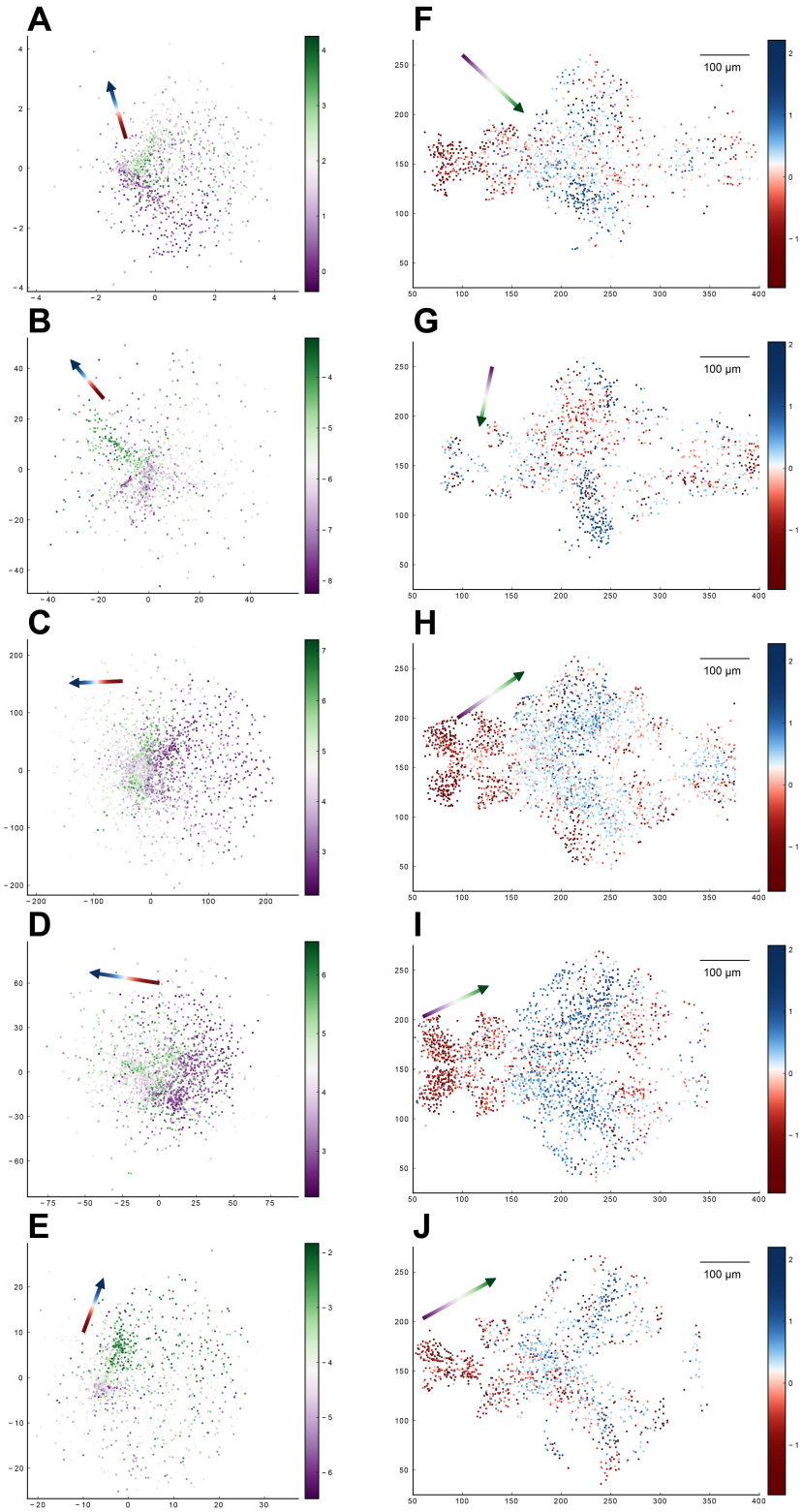

Figure S13. Relationship between the functional space and anatomical space for each zebrafish dataset from our experiments. Columns correspond to five light-field zebrafish data: fish 1 to fish 5 (with fish 6 has been shown in Fig. 6). **A-E.** Distribution of neurons in the functional space, where each neuron is color-coded by the projection of its coordinate along the canonical axis $\vec{b}_1$ in anatomical space (see text in Result section 2.6). Arrow: the first CCA direction $\vec{a}_1$ in functional space. **F-J.** Distribution of neurons in the anatomical space with the forebrain neuron located on the left side and the hindbrain neuron on the right side. Each neuron is color-coded by the projection of its coordinate along the canonical axis $\vec{a}_1$ in functional space (see text in Result section 2.6). Arrow: the first CCA direction $\vec{b}_1$ in anatomical space.

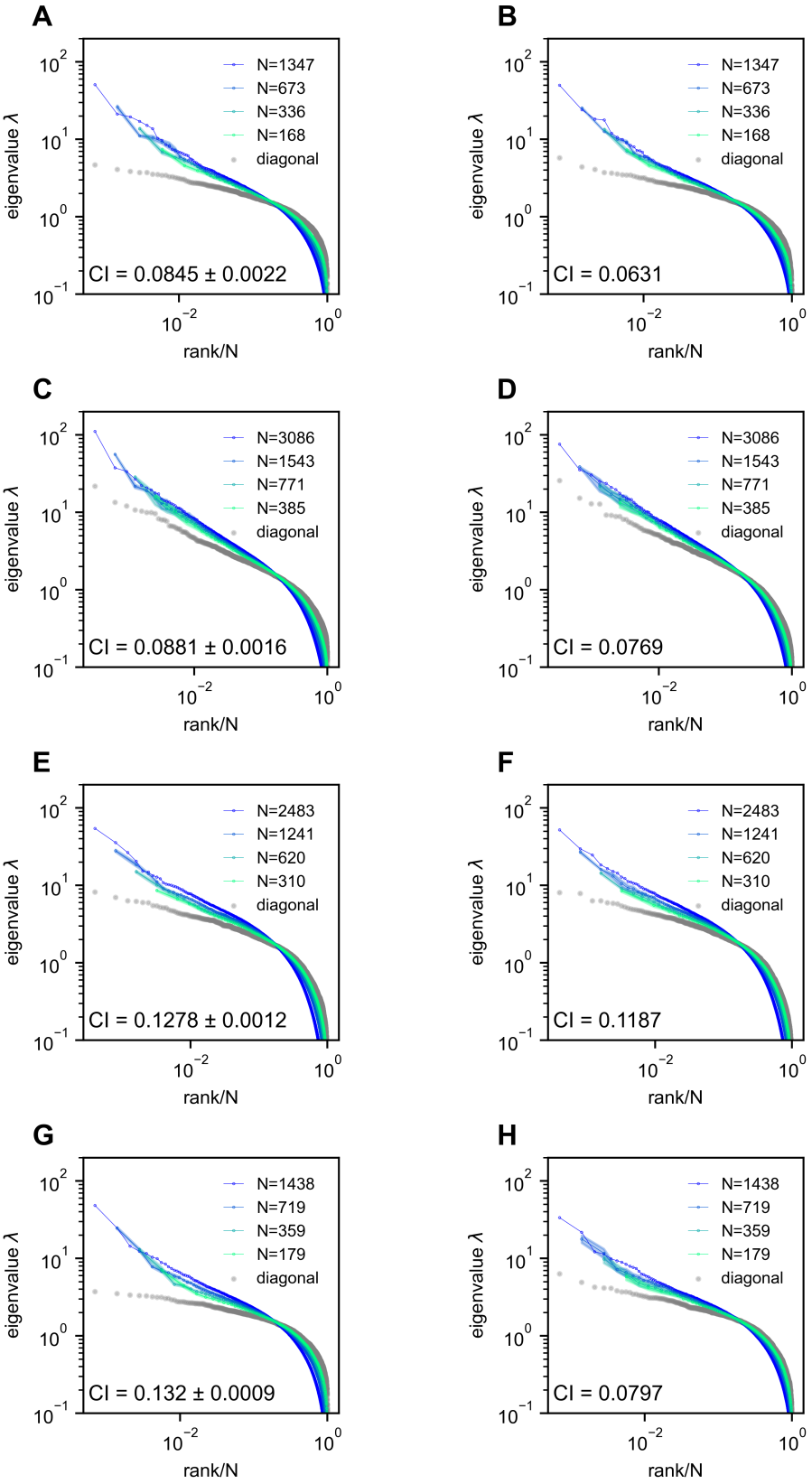

Figure S14. Removing the time segment of hunting behavior does not obliterate the scale-invariant eigenspectra. Rows correspond to 4 light-field zebrafish data: fish 2 to fish 5 (results for fish 1 has been shown in Fig. 7). **A,C,E,G.** Ctrl: we randomly remove the same number of time frames that are *not* the putative hunting frames. We repeat this process 10 times to generate 10 control covariance matrices and the CI is represented by mean±SD. **B,D,F,H.** Hunting removed: data obtained by removing hunting frames from the full data (S1). The CI for the hunting removed data appears to be significantly smaller than the control case (one-sample t-test $p = 2.2 \times 10^{-10}$ in fish 2, $p = 4.6 \times 10^{-9}$ in fish 3, $p = 1.7 \times 10^{-9}$ in fish 4, and $p = 3.4 \times 10^{-17}$ in fish 5).

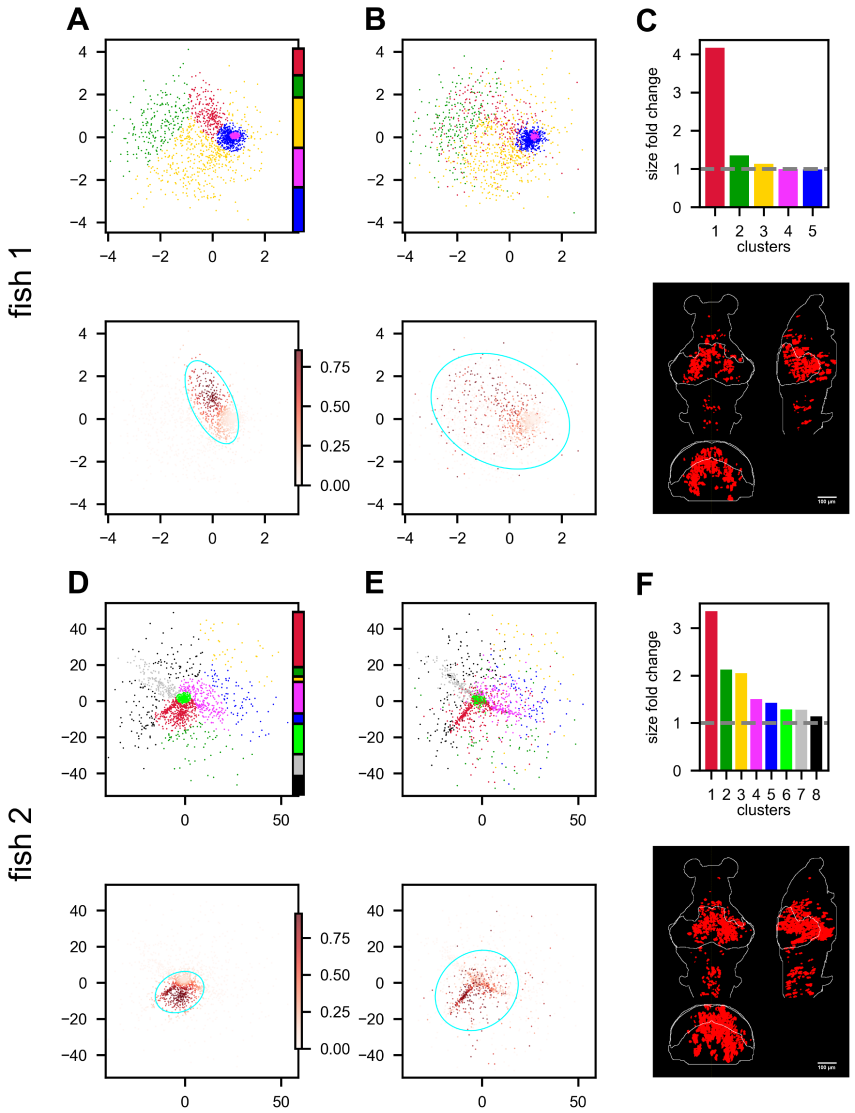

Figure S15. Hunting behavior reorganizes neurons in the functional space (continued on next page). Rows correspond to 5 light-field recordings of zebrafish engaged in hunting behavior: fish 1 to fish 5. **A,D,G,J,M. (top)** Functional space organization of the control data inferred by fitting the ERM and MDS (Methods section 2.6). Neurons are clustered using the Gaussian Mixture Models (GMMs) and their cluster memberships are shown by the color. The colorbar represents the proportion of neurons belonging to each cluster. **A,D,G,J,M. (bottom)** The coordinate distribution of the cluster in control data which is most dispersed (i.e., largest fold change in size, see below) after hunting-removal. The transparency of the dots (colorbar) is proportional to the probability of the neurons belonging to this cluster (S1). The cyan ellipse serves as a visual aid for the cluster size: it encloses 95% of the neurons belonging to that cluster (S1). **B,E,H,K,N. (top)** Similar to **A,D,G,J,M. (top)** but the functional coordinates are inferred from the hunting-removed data. The color-code of each neuron is the same as that in the control data, which allows for a comparison of the changes to the clusters under the hunting-removed condition. **B,E,H,K,N. (bottom)** Similar to **A,D,G,J,M. (bottom)** but the functional coordinates are inferred from the hunting-removed data. The transparency of each neuron is the same as in **A,D,G,J,M. (bottom)**, and it represents the probability p_{ik} (S1) of neurons belonging to the most dispersed cluster k in the control data. Likewise, the cyan ellipse encloses 95% of the neurons belonging to that cluster (S1). **C,F,I,L,O.** Top, size/area fold change (S1) for each cluster (the gray dashed line represents a fold change of 1, i.e., no change in size); bottom, the anatomical distribution of the neurons in the most dispersed cluster.

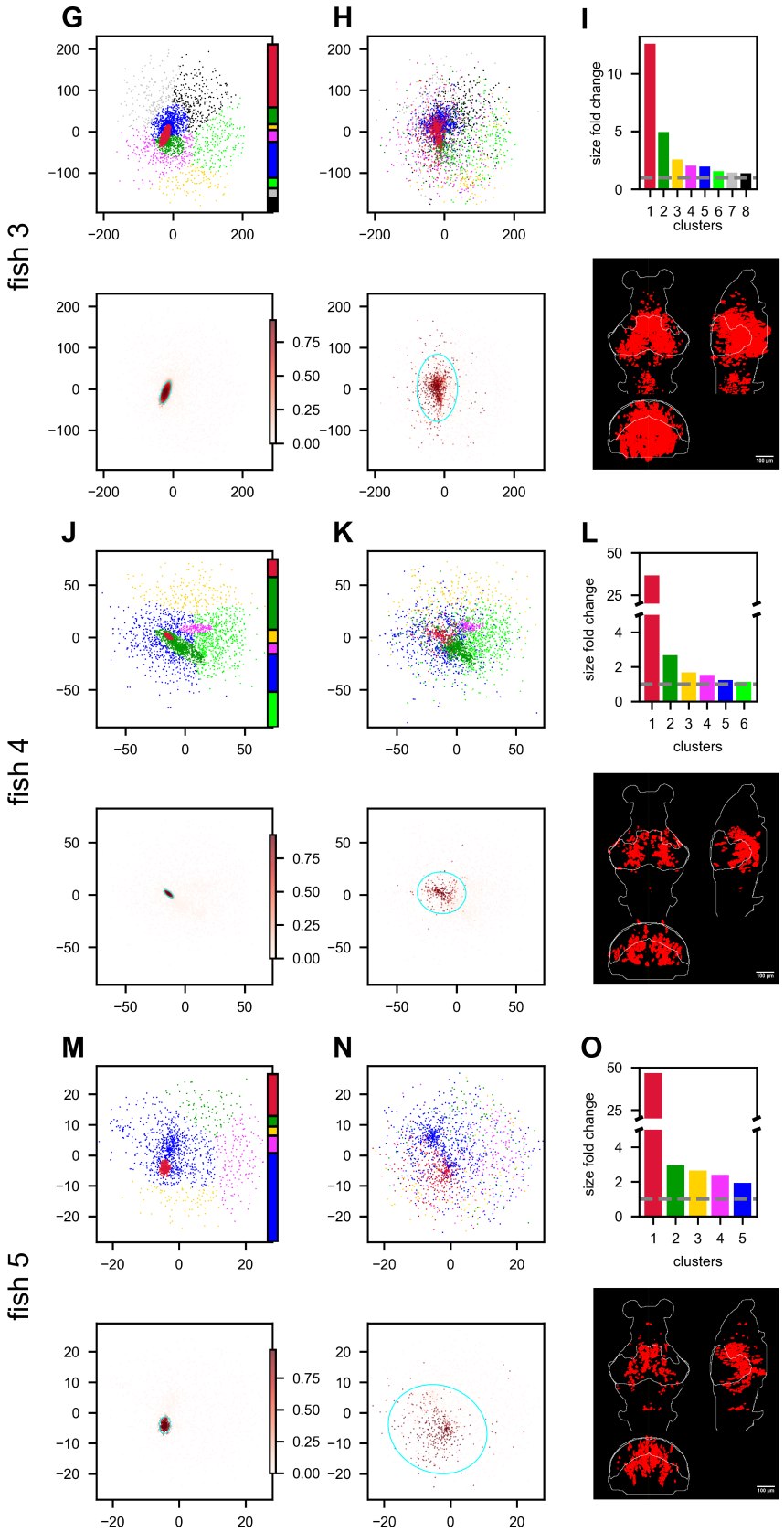

Figure S15. Hunting behavior reorganizes neurons in the functional space (continued).

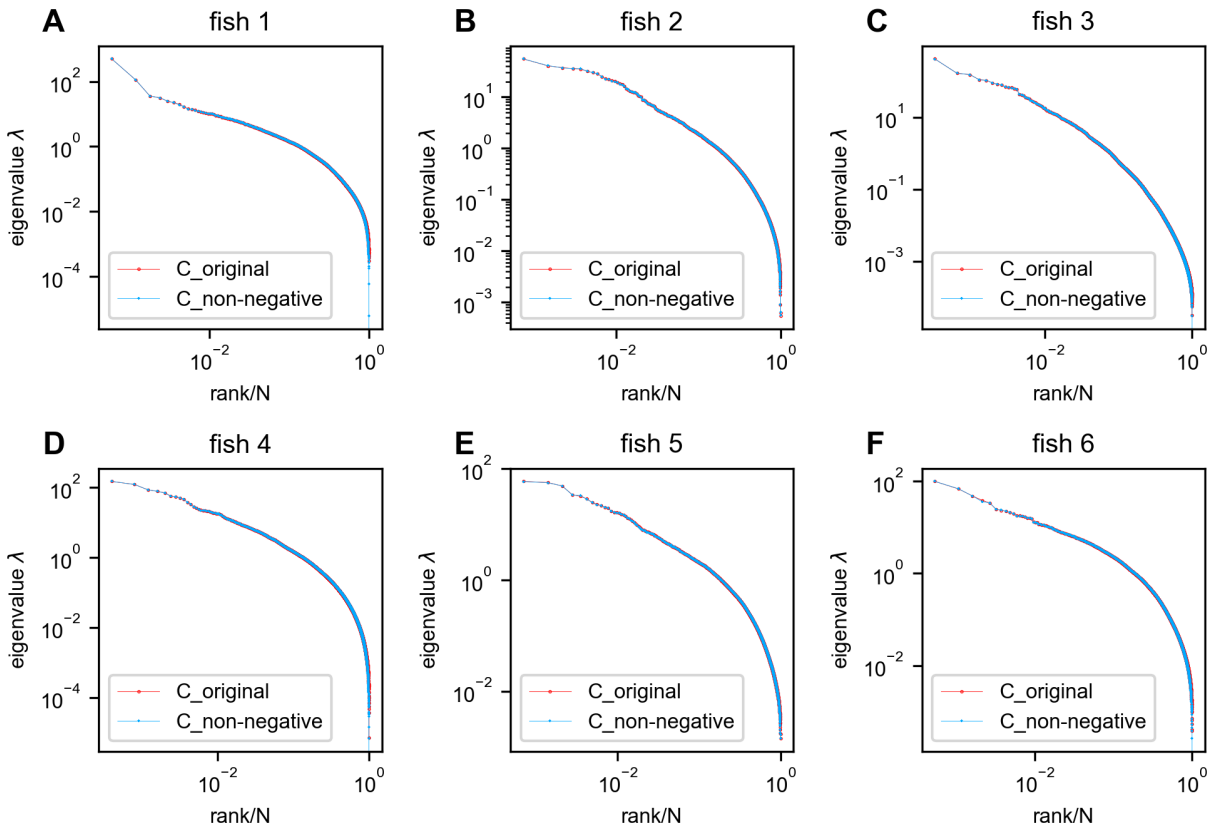

Figure S16. Negative covariances do not affect the eigenspectrum of the zebrafish data. Red: eigenspectrum of original data covariance matrix. Blue: eigenspectrum of the covariance matrix with negative entries replaced by zeros. In this figure, all neurons recorded in each fish were utilized without any subsampling.

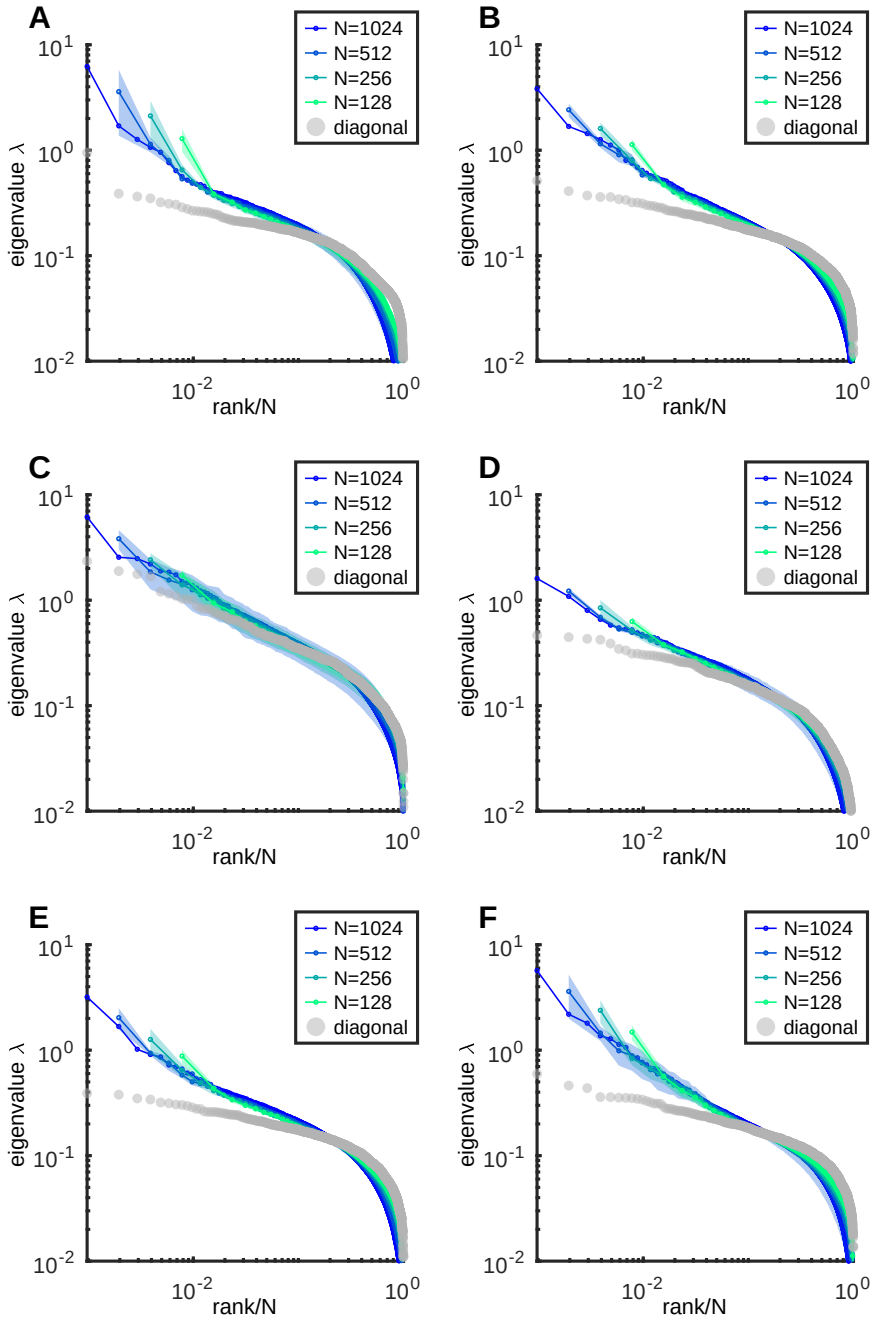

Figure S17. Eigenspectra of RG-inspired clustering in the zebrafish data. A-F fish 1 to fish 6. The clustering procedure follows the Renormalization-Group (RG) approach introduced in (32, 53). The cluster size is denoted by N, which is the number of neurons in each cluster. The standard error of the mean (SEM) across clusters is represented by the shaded area of each line.

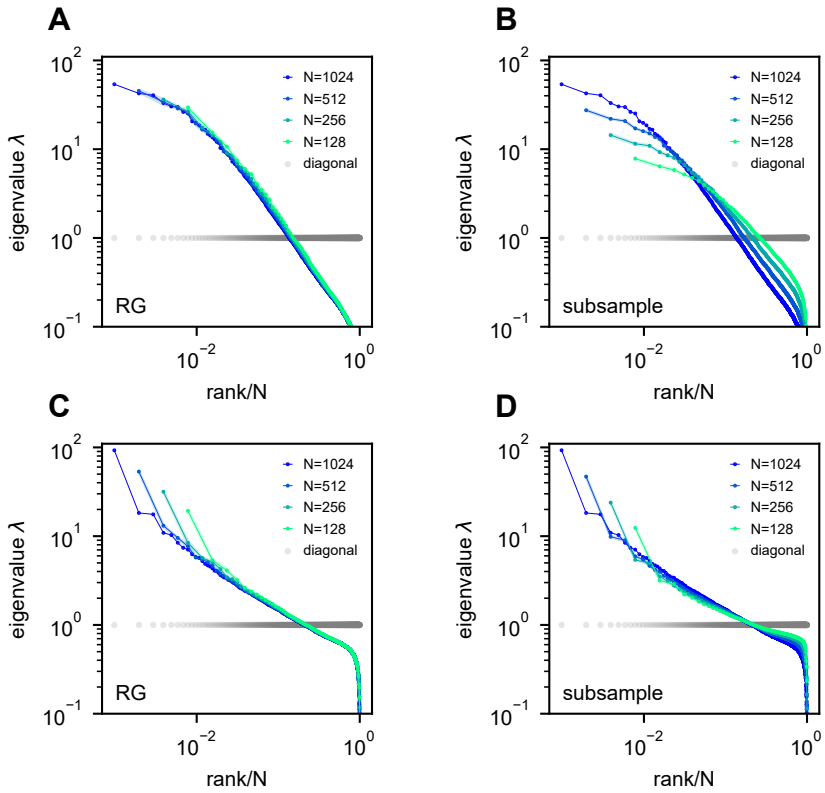

Figure S18. Eigenspectra of RG-inspired clustering and random subsampling in ERM. A,C. Clustered eigenspectra of ERM. The cluster size is denoted by N, which is the number of neurons in each cluster. We adopt the Renormalization-Group (RG) approach (32, 53), but with a specific modification (S1). Then we calculate the eigenspectra of covariance matrices across different cluster sizes, following the approach outlined in (32).**B,D.** Subsampled covariance eigenspectra of ERM. The standard error of the mean (SEM) across clusters is represented by the shaded area of each line. ERM parameters: **A,B** Exponential function $f(\vec{x}) = e^{-\|\vec{x}\|/b}$ where $b = 1$, $\rho = 10.24$ and dimension $d = 2$. **C,D** Approximate power law Eq. (2) with $\mu = 0.5$, $\rho = 10.24$ and dimension $d = 2$. Other parameters are the same as Fig. 2.